Plasma Sources
Science and
Technology

PAPER • **OPEN ACCESS**

Modeling of low-temperature argon plasma in capacitively-coupled glow discharges with a collisional-radiative model

To cite this article: Malamas Tsagkaridis *et al* 2025 *Plasma Sources Sci. Technol.* **34** 105013

OPEN ACCESS
IOP Publishing
Plasma Sources Science and Technology
Plasma Sources Sci. Technol. **34** (2025) 105013 (23pp)
https://doi.org/10.1088/1361-6595/ae0c33

Modeling of low-temperature argon plasma in capacitively-coupled glow discharges with a collisional-radiative model

Malamas Tsagkaridis[1,*], Todd A Oliver[1], Dan Fries[2], Ruairi O'Connor[3], Juan P Barberena-Valencia[3], Laxminarayan L Raja[3], Philip L Varghese[3] and Robert D Moser[1,4]

[1] Oden Institute for Computational Engineering and Sciences, The University of Texas at Austin, Austin, TX 78712, United States of America
[2] Department of Mechanical and Aerospace Engineering, University of Kentucky, Lexington, KY 40506, United States of America
[3] Department of Aerospace Engineering and Engineering Mechanics, The University of Texas at Austin, Austin, TX 78712, United States of America
[4] Department of Mechanical Engineering, The University of Texas at Austin, Austin, TX 78712, United States of America

E-mail: malamas.tsagkaridis@austin.utexas.edu

Received 6 April 2025, revised 16 September 2025
Accepted for publication 26 September 2025
Published 14 October 2025

Abstract

A comprehensive collisional-radiative model is developed and coupled with a one-dimensional two-temperature fluid model to study capacitively coupled radio-frequency argon discharges at pressures ranging from 0.5 to 5 Torr and electrode peak-to-peak voltages of 150 and 300 V. The fluid model is formulated using the drift-diffusion approximation. The CR model accounts for the argon ground state, 30 excited states in the 4 s, 4p, 3d, and 5 s manifolds, electrons, atomic (Ar^+) and molecular (Ar_2^+) ions, and argon excimer molecules (Ar_2^*). The processes included in the model are electron-impact excitation and ionization, radiation emission, heavy-particle collisions, radiative recombination, and processes involving Ar_2^+ and Ar_2^* molecules. Non-Maxwellian electron energy distribution functions, calculated using Bolsig+, are considered, with fine-structure collisional cross-sections acquired from the LXCat database. A detailed comparison is presented between numerical predictions and experimental measurements from a glow discharge device developed at UT Austin, focusing on populations of excited states in the 4p and 4 s manifolds, and electron number density. Additional comparisons are made with experimental data and PIC/Monte Carlo simulations from the study by (Donkó *et al* 2023 *Plasma Sources Sci. Technol.* **32** 065002). While agreement with the Donkó *et al* data is somewhat improved—particularly with the PIC/Monte Carlo results—the CR-fluid model systematically overpredicts the experimental values. Possible contributing

* Author to whom any correspondence should be addressed.

factors to these discrepancies and improvements to the model are discussed. In addition, the sensitivity of the results to the EEDF modeling is assessed by comparing simulations using Bolsig+-derived, Druyvesteyn, and Maxwellian distributions. The results show that predictions of electron temperature and plasma potential are strongly affected by the assumed EEDF shape. The inclusion of higher-lying excited states beyond the 4p manifold was found to have a minimal impact on discharge dynamics under the conditions studied. The code has been made publicly available on GitHub as open-source software.

Keywords: low-temperature plasmas, capacitively-coupled plasma (CCP), collisional-radiative model, argon, fluid modeling

1. Introduction

A capacitively coupled plasma (CCP) radio-frequency (RF) glow discharge is generated by applying an alternating voltage, typically at 13.56 MHz, to metallic or dielectric-coated electrodes (Raizer *et al* 1995). Low- and intermediate-pressure RF discharges find a wide range of applications in the microelectronics industry for plasma etching, thin film deposition, and surface modification (Rossnagel *et al* 1990, Bogaerts 1999). Furthermore, they are extensively employed in fundamental research on non-equilibrium plasma phenomena and plasma kinetics. Thus, it is desirable to develop models with predictive capabilities that can describe the behavior of such plasma discharges.

Glow discharges constitute weakly ionized gases maintained by external electric fields (Graves and Jensen 1986). The applied field, along with the low-energy transfer between electrons and heavier neutral species, results in highly energetic electrons (with temperatures of a few eV), while the neutral species remain nearly at ambient temperature. Several complex processes, such as charged-particle transport, plasma kinetics, and particle-surface interactions, occur in RF discharges. Electrons and ions interact with the applied electric field and diffuse toward the discharge chamber walls and electrodes (Raizer *et al* 1995), while ion impact at the electrodes induces secondary electron emissions (SEEs) in the plasma. Plasma kinetic processes include electron-impact excitation and ionization, emission and absorption of radiation, heavy-particle collision excitation and ionization, and radiative recombination.

Many techniques have been used to experimentally measure properties of low-temperature plasmas (Ochkin 2009, Engeln *et al* 2020). Of relevance to this work are optical emission spectroscopy (OES), laser absorption spectroscopy (LAS), and Langmuir probe measurements. OES and LAS provide information about the population densities of excited species within the plasma. Several studies have employed absolute radiance calibrated OES to infer densities of high lying excited states using the natural emission of light from the plasma, the intensity of the emission line being proportional to the population of the emitting state (Ferrari 1965, Lipka *et al* 2007, O'Connor *et al* 2025). LAS has also been used extensively to infer population densities of excited states from the absorption of laser light due to the presence of a specific species (McMillin and Zachariah 1995, Augustyniak *et al* 1999, Grigorian *et al* 2015, Peshl *et al* 2019). Both of these optical diagnostics are well-established non-intrusive techniques. Langmuir probes are one of the oldest plasma diagnostic and provide a wealth of information at the cost of being intrusive to the plasma (Mott-Smith and Langmuir 1926, Chen 2012, Godyak and Alexandrovich 2015). This technique allows measurement of electron density, electron temperature and even the EEDF (Druyvesteyn 1930, Godyak 1990, Godyak *et al* 2002). All three of these diagnostics have been employed in this study to provide benchmarking data for our simulations.

Several mathematical models have been developed to describe plasma physics in glow discharges from various perspectives. They can be broadly categorized into three classes (Lymberopoulos and Economou 1993, Bogaerts 1999): kinetic, continuum, and hybrid models. Kinetic models employ the Boltzmann transport equation (Hagelaar and Pitchford 2005, Fernando *et al* 2024) or particle-in-cell (PIC) / Monte Carlo methods (Bogaerts and Gijbels 1999, Verboncoeur 2005, Donko 2011, Gudmundsson *et al* 2021)to fully predict the evolution of the electron energy distribution function (EEDF), albeit at a high computational cost. Continuum or fluid models, on the other hand, solve equations for the moments of the distribution function in the Boltzmann equation (Gogolides and Sawin 1992), lowering the computational cost but also the physical fidelity. Recent advancements have introduced high-order moment closures to improve the accuracy of fluid models (Laguna *et al* 2023, Alvarez Laguna *et al* 2024). Hybrid models typically utilize a PIC/Monte Carlo method for electrons and ions while employing a fluid model to describe the behavior of neutral species (Bogaerts *et al* 1999, Kushner 2009, Economou 2017, Wen *et al* 2019, Donko *et al* 2023, Fernando *et al* 2025). This work focuses on the fluid description, which applies to discharges with low Knudsen numbers, meaning the electron mean free path is much smaller than the characteristic discharge dimension (Gogolides and Sawin 1992). This condition is typically met for discharges operating in the pressure range of approximately 0.1 to 5 Torr (Graves and Jensen 1986, Liu *et al* 2014, Gudmundsson *et al* 2021).

Fluid models for RF glow discharges date back to the original work of Graves and Jensen (1986), who developed

a one-dimensional (1D) fluid model incorporating equations for electron and ion continuity, Poisson's equation for the electric field, and an electron energy equation. Subsequent work by Graves (1987) demonstrated that this model can qualitatively reproduce experimentally observed features in RF discharges, highlighting the potential of fluid models in describing discharge physics. Gogolides and Sawin (1992) provided a rigorous mathematical derivation of a fluid model from the moments of the Boltzmann equation, discussed the fundamental assumptions underlying the fluid equations, and proposed an equation for ions that incorporates an effective electric field.

Around the same time, Lymberopoulos and Economou (1993) developed a 1D fluid model for argon discharges and incorporated reactive transport equations for neutral metastable species. Their analysis showed that metastables play a crucial role in discharge physics at ≈ 1 Torr pressures, with step-wise electron-impact ionization identified as the dominant electron production mechanism. Later, Deng *et al* (2008) employed a similar 1D fluid approach to study non-equilibrium processes during breakdown in an Ar glow discharge. Similarly, Liu *et al* (2014) studied the effect of SEE on the discharge characteristics, while Liu *et al* (2017) investigated pulsed RF discharges. Capacitively RF argon glow discharges at various pressures were also studied with a 1D fluid model by Samir *et al* (2018), while Gao *et al* (2021) studied glow discharges at low pressures ranging from 60 to 140 mTorr.

Most fluid glow-discharge Ar models reported to date either neglect the internal kinetic processes of neutral species or employ a simplified description based on 'lumped' species, i.e. metastables. These lumped species represent effective excited states rather than accounting for the fine structure states. A more comprehensive description of the population dynamics of atomic or molecular energy levels can be achieved with a collisional-radiative (CR) model. Detailed CR models, also known as state-to-state, or population kinetics models, are widely used in plasma spectroscopy, i.e. OES (Zhu and Pu 2011, Akatsuka 2019), to analyze plasma kinetics and emission spectra under conditions far from local thermodynamic equilibrium.

CR models have been investigated extensively (Ralchenko 2016), with numerous studies documented in the literature. An early review of CR models and their classification for different types of plasmas was conducted by Van Sijde *et al* (1984). Many studies on argon CR models are based on the pioneering work of Katsonis and Drawin (1980), Vlcek (1989)and Vlvek and Pelikan (1989). Apart from electron-impact excitation/ionization and radiative processes, these studies included formulations for atom–atom inelastic collisional processes based on hydrogenic approximations, while a Maxwellian energy distribution was assumed for the electron and atom energy distribution functions (EEDF). Bogaerts *et al* (1998) extended Vlcek's Ar CR model and used a Monte-Carlo method to solve the EEDF. 64 argon excited levels were incorporated in the model, while particular emphasis was given to the description of atom-induced processes. The model was coupled with a 1D fluid model and used to simulate a direct current (DC) glow discharge cell. Kapper and Cambier (2011) developed a detailed CR model that included all individual excited states up to the Ar(3d) and Ar(5 s) manifolds. This model was coupled with a 1D two-temperature fluid transport model to simulate ionizing shocks in argon. Similarly, Gangwar *et al* (2012) developed a 0D CR model for Ar that also incorporated a complete fine-structure description of the electron-impact excitation process. Finally, Chung *et al* (2021) considered the most recent atomic data available for argon in the literature and from various sources to construct a CR model. Particular emphasis was given to the uncertainties associated with atomic datasets for the high-lying excited states.

Recently, Donko *et al* (2023, 2024) developed a CR model coupled with a 1D PIC/Monte Carlo method to study argon CCP RF discharges at low pressures ranging from 5 to 150 Pa. This work is likely the first to compare simulation data for the $1s5$ metastable state with spatially resolved experimental measurements. Overall, the computational and experimental results for the $1s5$ state showed good qualitative and quantitative agreement. Discrepancies increased with increased pressure and were attributed to the effect of line-of-sight integration inherent in the experimental technique and uncertainties in the input data of the model.

While the sophistication of fluid models for argon CCP RF glow discharges has increased over the years, they usually use a simplified description of plasma kinetics, well below the fidelity of a CR model. Moreover, comparisons of numerical predictions with experimental data for species and electron number densities are rare. Thus, the purpose of the present article is twofold. First, we develop a 1D two-temperature fluid model and couple it with a detailed general-purpose argon CR model to describe capacitively coupled RF glow discharges. Second, we compare the numerical predictions with experimental data for the number densities of excited states, in the 4 s and 4p manifolds, and electrons.

The simulations consistently overpredicted the experimental data for all operating conditions analyzed in this study. We examine sources of uncertainty and limitations in the current methodology, discuss possible contributing factors to discrepancies, and outline directions for model improvement.

The rest of the article is structured as follows: Initially, we introduce the governing equations and primary assumptions underlying the fluid model. This is followed by a detailed description of the CR model adopted in this study. Next, we explain the numerical solution method. We then present and discuss the results and conclude the article with a summary of the main findings.

2. Mathematical formulation

2.1. Fluid model

The fluid model consists of a set of coupled partial differential equations (PDEs) that govern the species number densities, energy, and electric potential. These PDEs and the required closures are based on the following modeling assumptions:

- The discharge electrode diameter is larger than the electrode spacing, allowing for a 1D approximation in which plasma properties vary only along the direction perpendicular to the electrode planes.
- A two-temperature model is utilized, assuming a common temperature, T_g, for all heavy species and a separate temperature, T_e, for electrons. The ion temperature is set equal to that of the neutral species.
- The drift-diffusion approximation describes the ion and electron fluxes, utilizing a quasi-steady-state form of the momentum balance equation. This approach is typically justified for electrons, as their effective momentum transfer frequency ν_m, calculated from mobility data, is much higher than the discharge driving frequency. However, this simplification may not be valid for ions (Gogolides and Sawin 1992), which will be discussed further in section 4.2.
- Data for the EEDF are computed in advance and tabulated for subsequent use. This approach is discussed in more detail in section 2.2.
- A quasi-static model is employed to describe the electromagnetic field driving the discharge. Magnetic field effects are negligible.

For a detailed discussion on the fundamental assumptions of glow discharge models, we refer to Graves and Jensen (1986), Lymberopoulos and Economou (1993) and Raizer *et al* (1995).

With these assumptions, we can formulate governing equations for the species number densities, energies, and electric potential. The species transport equations are as follows:

$$\frac{\partial n_\alpha}{\partial t} + \frac{\partial F_\alpha}{\partial x} = \dot{\omega}_\alpha, \tag{1}$$

where t is time, x is the coordinate in the electrode-normal direction, n_α denotes the number density of species α, F_α is the corresponding flux, and $\dot{\omega}_\alpha$ is the net production rate of species α due to plasma kinetic processes. For clarification, the term 'species' refers to any of the following: ground state atoms, excited states of Ar, electrons, atomic and molecular argon ions, and argon excimer molecules. The species production rates are governed by the kinetics model given in section 2.3. The species flux is closed assuming drift and Fickian diffusion:

$$F_\alpha = z_\alpha \mu_\alpha n_\alpha E - D_\alpha \frac{\partial n_\alpha}{\partial x}, \tag{2}$$

where z_α is the charge number (zero for neutrals), μ_α is the mobility, D_α is the diffusion coefficient, and E is the electric field. The transport properties are described in section 2.2. The electric field is determined from the potential, $E = -\frac{\partial \phi}{\partial x}$, which is governed by a Poisson equation (defined in equation (5)). The formulation in equation (2) neglects transient effects, which is typically valid for electrons but may not hold for heavier ions that do not respond instantaneously to the external electric field, E. To account for this, Gogolides *et al* (1992), Gogolides and Sawin (1992) proposed replacing E in equation (2) with an effective electric field, E^{ef}, acting on the ions, defined by:

$$\frac{\partial E^{ef}}{\partial t} = \nu_m \left(E - E^{ef}\right), \tag{3}$$

where $\nu_m = \frac{q_e}{m_+ \mu_+}$ is the ion momentum transfer frequency, q_e is the elementary charge (i.e. the magnitude of the electron charge), m_+ is the ion mass, and μ_+ represents the ion mobility. The treatment of the argon ground state, also referred to as the background species, under the constraint of constant pressure is discussed in appendix A.

A two-temperature model is adopted in this study. We assume a common temperature T_g for the heavy species, including ions, and a separate temperature T_e for the electrons. Defining the electron energy density as $n_e e_e = \frac{3}{2} k_B n_e T_e$, the electron energy equation is given by:

$$\frac{\partial}{\partial t}\left(\frac{3}{2}k_B n_e T_e\right) + \frac{\partial}{\partial x}\left(\frac{5}{2}k_B T_e F_e - \kappa_e \frac{\partial T_e}{\partial x}\right) = \underbrace{-q_e F_e E}_{\text{Joule heating}} + \underbrace{\dot{\omega}_{e_e}}_{\text{Plasma kinetics}}, \tag{4}$$

where n_e denotes the electron number density, k_B is the Boltzmann constant, κ_e is the electron thermal conductivity, and $\dot{\omega}_{e_e}$ is the net production rate of electron energy due to plasma kinetic processes, as defined in equation (18) and discussed in section 2.3. The flux is closed as described in equation (2).

A quasi-static model is used to describe the electromagnetic field driving the discharge. Thus, Maxwell's equations reduce to a Poisson equation governing the electric potential ϕ:

$$-\frac{\partial^2 \phi}{\partial x^2} = \frac{\rho_c}{\epsilon_0}, \tag{5}$$

where ρ_c is the charge density and ϵ_0 is the permittivity of free space. The charge density can be computed from the species densities:

$$\rho_c = \sum_{\alpha=1}^{N_s} z_\alpha q_e n_\alpha, \tag{6}$$

where N_s is the number of species considered in the model.

To solve the system of equations, suitable boundary conditions have to be defined at each electrode. For a 1D simulation, we define the grounded anode electrode as $x = 0$ and the powered cathode electrode as $x = L$. We impose conditions on the electron and ion fluxes on both sides. The electron flux F_e is given by:

$$F_e \mathbf{n}_x = \frac{1}{4} n_e \overline{v_e} - \sum_{\alpha=1}^{N_s} \gamma_\alpha F_\alpha \mathbf{n}_x, \tag{7}$$

where $\mathbf{n}_x$ denotes the outward-pointing unit normal vector ($\mathbf{n}_x = -1$ at $x = 0$ and $\mathbf{n}_x = 1$ at $x = L$), and $\overline{v_e} = \left(\frac{8 k_B T_e}{\pi m_e}\right)^{1/2}$ represents the mean thermal velocity of electrons, where m_e is the electron mass. The SEE coefficient, γ_α, for species α is assumed to be the same for all ion species considered in

the model, namely Ar^+ and $Ar_2{}^+$, and zero for neutral species. For ions, it is assumed that the ion flux to the electrodes is primarily driven by the electric field (drift-diffusion flux), with the normal diffusion flux considered negligible. This results in a condition equivalent to a Neumann boundary condition, $\frac{\partial n_+}{\partial x} = 0$. Specifically, the ion flux, F_+, is given by:

$$F_+ \mathbf{n}_x = \max\left(0, n_+ \mu_+ E \mathbf{n}_x\right), \tag{8}$$

Here, F_+, n_+, and μ_+ represent the ion flux, ion number density, and ion mobility, respectively, and refer to either Ar^+ or $Ar_2{}^+$ ions. Dirichlet boundary conditions are applied for all neutral species, with the ground-state density given by $n_\mathrm{b}(0,t) = n_\mathrm{b}(L,t) = \frac{P}{k_\mathrm{B} T_\mathrm{g,w}}$ and the densities of all other neutral species set to zero, $n_\alpha(0,t) = n_\alpha(L,t) = 0$. Here, n_b denotes the number density of the argon ground state, P is the pressure, and $T_\mathrm{g,w}$ represents the wall temperature. Additionally, Dirichlet conditions are imposed on the electric potential on both sides. Specifically, the electric potential for the RF glow discharge at the two electrodes is:

$$\phi(0,t) = 0, \quad \phi(L,t) = V_0 \sin(2\pi f t), \tag{9}$$

where V_0 is the voltage amplitude and f is the frequency. For the electron energy equation, the total surface energy flux at the electrodes is given by:

$$Q_\mathrm{e,s} \mathbf{n}_x = \frac{5}{2} k_\mathrm{B} T_\mathrm{e} \left(\frac{1}{4} n_\mathrm{e} \overline{v_\mathrm{e}}\right) - \sum_{\alpha=1}^{N_\mathrm{s}} \gamma_\alpha F_\alpha \epsilon_\mathrm{s} \mathbf{n}_x, \tag{10}$$

where $\epsilon_\mathrm{s} = \frac{3}{2} k_\mathrm{B} T_\mathrm{e,s}$ is a fixed electron energy prescribed for the emitted electrons. Finally, isothermal wall conditions are imposed for the gas temperature.

2.2. EEDFs and transport properties

The zero-dimensional electron Boltzmann equation solver, Bolsig+ (Hagelaar and Pitchford 2005), is employed to determine the EEDF and the mean electron energy over a range of reduced electric field values, $\frac{E}{n_\mathrm{b}}$. Here, n_b denotes the number density of the background species, i.e. the argon ground state. The input parameters in the solver include cross-sections for electron-impact processes and the gas composition. The resulting data are then mapped to the electron temperature T_e via the mean electron energy and stored for subsequent use. A similar one-to-one mapping between $\frac{E}{n_\mathrm{b}}$ and T_e was utilized by Mahadevan and Raja (2010), as detailed in appendix A of their work. Furthermore, this study also investigates the use of a Maxwellian EEDF, expressed as (Mitchner and Kruger Jr 1973):

$$f_\mathrm{M}(\epsilon) = 2\sqrt{\frac{\epsilon}{\pi}} \left(\frac{1}{k_\mathrm{B} T_\mathrm{e}}\right)^{\frac{3}{2}} \exp\left(-\frac{\epsilon}{k_\mathrm{B} T_\mathrm{e}}\right), \tag{11}$$

and a Druyvesteyn EEDF, expressed as (Tiwari *et al* 2023):

$$f_\mathrm{Dn}(\epsilon) = \sqrt{2}\zeta\sqrt{\epsilon} \left(\frac{1}{k_\mathrm{B} T_\mathrm{e}}\right)^{\frac{3}{2}} \exp\left(-\alpha \left(\frac{\epsilon}{k_\mathrm{B} T_\mathrm{e}}\right)^2\right). \tag{12}$$

In these expressions, ϵ represents the electron kinetic energy, and the parameters α and ζ are given by $\alpha = \frac{\Gamma(1/4)^4}{72\pi^2}$ and $\zeta = \frac{1}{\sigma} \cdot \frac{\Gamma(1/4)^3}{\Gamma(3/4)}$, where $\Gamma(x)$ is the Gamma function and $\sigma = 6\sqrt{3} \cdot 2^{3/4} \cdot \pi^{3/2}$.

Figure 1 presents EEDFs calculated using Bolsig+, Maxwellian, and Druyvesteyn distributions for electron temperatures ranging from 2 to 7 eV. At lower electron temperatures (e.g. $T_\mathrm{e} = 2$ eV), the Bolsig+ distribution is significantly depleted at higher electron energies compared to the Maxwellian, reflecting strong non-equilibrium effects. As the temperature increases, the Bolsig+ EEDF gradually approaches the Maxwellian distribution.

Experimental data for the mobility of charged species, including electrons, were obtained from the LXCat database (https://nl.lxcat.net/home/, accessed in January 2023). Specifically, the electron mobility, μ_e, used in equation (2), is sourced from Hernandez-Avila *et al* (2004), Alves (2014) and is expressed as a function of temperature. The argon ion mobility, μ_{Ar^+}, is taken from Ellis *et al* (1976), Helm and Elford (1977), Hegerberg *et al* (1982), Phelps (1991), Viehland and Kirkpatrick (1995), Phelps and Petrovic (1999). Based on these data, we performed a fit leading to the following expression:

$$\mu_{Ar^+} n_\mathrm{b} = \frac{4.11 \cdot 10^{21}}{\left[1 + \left(0.008\,916 \cdot \frac{E}{n_\mathrm{b}}\right)^{1.595}\right]^{0.2721}}, \tag{13}$$

where $\frac{E}{n_\mathrm{b}}$ is in Td and $\mu_\mathrm{Ar}^+ \;\; n_\mathrm{b}$ is in $1/(\mathrm{V\,m\,s})$. The mobility of the argon molecular ion, $\mu_{Ar_2{}^+}$, is obtained from Viehland and Kirkpatrick (1995). The electron and ion diffusion coefficients are determined using the Einstein–Smoluchowski relation (Lieberman and Lichtenberg 2005), as expressed by:

$$D_\alpha = \frac{k_\mathrm{B} T_\alpha \mu_\alpha}{q_\mathrm{e} z_\alpha}. \tag{14}$$

A constant value is used for the diffusion coefficient of the argon excited states, as the temperature of the heavy species does not change significantly. The electron thermal conductivity is approximated as:

$$\kappa_\mathrm{e} = \frac{5}{2} n_\mathrm{e} k_\mathrm{B} D_\mathrm{e}. \tag{15}$$

2.3. Plasma kinetics

The CR formulation adopted in this study is based on the work of Kapper and Cambier (2011), Chung *et al* (2021), and the CR studies outlined in the introduction. Specifically, the model incorporates the first 14 atomic energy levels

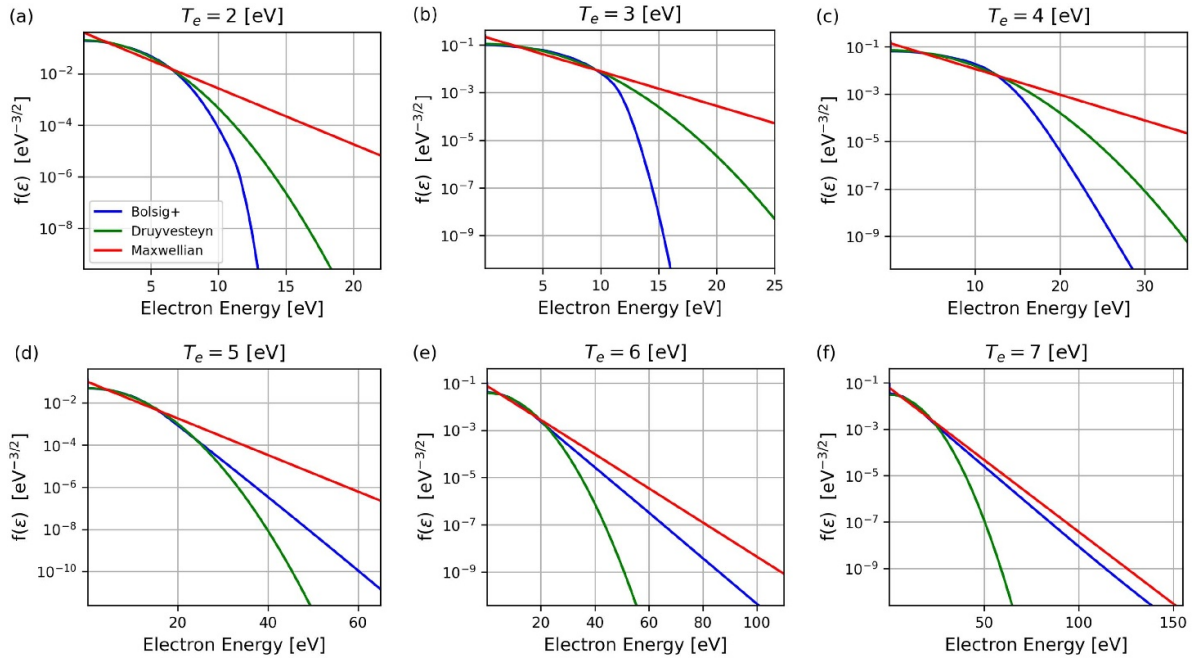

Figure 1. EEDFs computed using Bolsig+, Maxwellian, and Druyvesteyn distributions at different electron temperatures, T_e, ranging from 2 to 7 eV. A logarithmic scale was used for the vertical axis.

Ar(i) of neutral argon (i.e. excited states for the 4 s and 4p manifolds), the argon ground state Ar(1), electrons e^-, the ground state of the singly-charged atomic ions Ar^+, molecular ions $Ar_2{}^+$, and argon excimer molecules $Ar_2{}^*$. Furthermore, the possibility of using the first 30 atomic energy levels of neutral argon (i.e. the 4 s, 4p, 3d, and 5 s manifolds) is explored to investigate the effect of higher-lying excited states, as discussed in section 4.5.2. The atomic energy levels of neutral argon are obtained from the National Institute of Standards and Technology (NIST) atomic spectra database (Kramida *et al* 2023) (https://physics.nist.gov/PhysRefData/ASD/levels_form.html accessed in January 2023). No levels are lumped together in this study, as the methodology focuses on examining the influence of electronic states in detail. The plasma kinetic processes incorporated into the model are listed below[5]:

I. Electron-impact excitation / de-excitation
$$\mathrm{Ar}(i) + \mathrm{e}^-(\epsilon) \overset{F_{ji}}{\rightleftharpoons} \mathrm{C}_{ij}\mathrm{Ar}(j) + \mathrm{e}^-(\epsilon - \varepsilon_{ij})$$
II. Electron-impact ionization / three-body recombination
$$\mathrm{Ar}(i) + \mathrm{e}^-(\epsilon) \overset{Q_i}{\rightleftharpoons} \mathrm{S}_i\mathrm{Ar}^+ + \mathrm{e}^-(\epsilon - \varepsilon_{Ii}) + \mathrm{e}^-$$
III. Spontaneous emission and radiation trapping with escape factors
$$\mathrm{Ar}(i) + \mathrm{h}\,\nu_{ij} \underset{\eta_{ji}\ \mathrm{A}_{ji}}{\longleftarrow\!\!\!\!\!\!\!\!} \mathrm{Ar}(j) \text{ for } i < j$$
IV. Atom-impact excitation / de-excitation
$$\mathrm{Ar}(i) + \mathrm{Ar}(1) \overset{L_{ji}}{\rightleftharpoons} \mathrm{K}_{ij}\mathrm{Ar}(j) + \mathrm{Ar}(1)$$
V. Atom-impact ionization / three-body recombination
(a) $\mathrm{Ar}(i) + \mathrm{Ar}(1) \overset{W_i}{\rightleftharpoons} \mathrm{V}_i\mathrm{Ar}^+ + \mathrm{e}^- + \mathrm{Ar}(1)$
(b) $\mathrm{Ar}(i) + \mathrm{Ar}(j) \xrightarrow{\mathrm{K}^{\mathrm{I}}_{ij}} \mathrm{Ar}^+ + \mathrm{e}^- + \mathrm{Ar}(1)$ (Only for the 4 s states)
VI. Photoionization / Radiative recombination
$$\mathrm{Ar}(i) + \mathrm{h}\,\nu \underset{\mathbf{\Lambda}_i\ \mathrm{R}_i}{\longleftarrow\!\!\!\!\!\!\!\!} \mathrm{Ar}^+ + \mathrm{e}^-$$
VII. Argon molecular ion, $Ar_2{}^+$, processes
(a) Atomic to molecular ion conversion
$\mathrm{Ar}^+ + \mathrm{Ar}(1) + \mathrm{Ar}(1) \xrightarrow{\mathrm{K_{MC}}} \mathrm{Ar}^{2+} + \mathrm{Ar}(1)$
(b) metastable-metastable associative ionization
$\mathrm{Ar}(3\mathrm{p}^5 4\mathrm{s}) + \mathrm{Ar}(3\mathrm{p}^5 4\mathrm{s}) \xrightarrow{\mathrm{K_{MAI}}} \mathrm{Ar}_2^+ + \mathrm{e}^-$
(c) dissociative recombination
$\mathrm{Ar}_2^+ + \mathrm{e}^- \xrightarrow{\mathrm{K_{DR}}} \mathrm{Ar}(1) + \mathrm{Ar}(1)$
(d) dissociative recombination
$\mathrm{Ar}_2^+ + \mathrm{e}^- \xrightarrow{\mathrm{K_{DR*}}} \mathrm{Ar}(2 \leqslant \mathrm{i} \leqslant 4) + \mathrm{Ar}(1)$
(e) direct electron dissociation
$\mathrm{Ar}_2^+ + \mathrm{e}^- \xrightarrow{\mathrm{K_{DD}}} \mathrm{Ar}^+ + \mathrm{Ar}(1) + \mathrm{e}^-$
VIII. Excimer molecule, $Ar_2{}^*$, processes
(a) metastable association
$\mathrm{Ar}(3\mathrm{p}^5 4\mathrm{s}) + \mathrm{Ar}(1) + \mathrm{Ar}(1) \xrightarrow{\mathrm{K_{MA}}} \mathrm{Ar}_2^* + \mathrm{Ar}(1)$
(b) electron impact dissociation
$\mathrm{Ar}_2^* + \mathrm{e}^- \xrightarrow{\mathrm{K_{ED}}} \mathrm{Ar}(3\mathrm{p}^5 4\mathrm{s}) + \mathrm{Ar}(1) + \mathrm{e}^-$
(c) molecule—metastable impact ionization
$\mathrm{Ar}_2^* + \mathrm{Ar}(3\mathrm{p}^5 4\mathrm{s}) \xrightarrow{\mathrm{K_{MMI}}} \mathrm{Ar}(1) + \mathrm{e}^- + \mathrm{Ar}_2^+$
(d) molecular impact ionization
$\mathrm{Ar}_2^* + \mathrm{Ar}_2^* \xrightarrow{\mathrm{K_{MI}}} \mathrm{Ar}(1) + \mathrm{Ar}(1) + \mathrm{e}^- + \mathrm{Ar}_2^+$
(e) radiative dissociation
$\mathrm{Ar}_2^* \xrightarrow{\mathrm{A}_{\mathrm{Ar}_2{}^*}} \mathrm{Ar}(1) + \mathrm{Ar}(1) + \mathrm{hv}$

[5] The 1*s*5 and 1s3 argon states (in Paschen notation) are commonly referred to as the metastable (*m*) states, while the 1*s*2 and 1*s*4 states are referred to as the resonance (*r*) states.

The electron kinetic energy is denoted as ϵ, ε_i is the atomic energy of the excited states of the *i*th energy level Ar*(i)*, $\varepsilon_{ij} = \varepsilon_j - \varepsilon_\mathrm{i}$ is the energy difference between the upper and lower levels, and $\varepsilon_{\mathrm{I}i} = \varepsilon_\mathrm{I} - \varepsilon_\mathrm{i}$ is the ionization potential of the *i*-th energy level, with ε_I being the ionization energy of argon ground state[6]. We follow the rate coefficient notation of Vlcek (1989): C_{ij} and F_{ji} represent the rate coefficients for collisional excitation and de-excitation by electrons, respectively. S_i denotes the rate coefficient for electron-impact ionization, and Q_i for the three-body recombination. A_{ji} is the Einstein coefficient for spontaneous emission from the *j*th to *i*th level, h is the Planck constant, ν is the photon frequency, and $\eta_{ji} \in (0,1)$ is the optical escape factor. K_{ij}, V_i, L_{ji}, and W_i represent the rate coefficients for excitation and ionization via collisions with ground state atoms and the corresponding reverse processes. K^I_{ij} denotes the rate coefficient for ionization due to collisions between excited states in the 4 s manifold. Finally, R_i denotes the radiative recombination rate coefficient, and Λ_i is the optical escape factor for free-bound transitions.

The net production rate, $\dot{\omega}_\mathrm{i}$, of the *i* th argon species due to plasma kinetic processes is described in equation (16), where n_i is the number density of the *i*th energy level[7], n_{Ar_+} is the atomic ion number density, $n_1 \equiv n_\mathrm{b}$ is the number density of the background species (i.e. the argon ground state Ar(1)), and c_j is a constant such that $c_j = 2$ for $j = i$ and $c_j = 1$ otherwise. The net production rate for electrons is given in equation (17). The terms S^m_i and S^m_e represent the contributions from processes involving the $Ar_2{}^+$ and $Ar_2{}^*$ species (processes VII. and VIII.).

$$\begin{aligned}\dot{\omega}_\mathrm{i} \equiv \left.\frac{\partial n_\mathrm{i}}{\partial t}\right|_\mathrm{kinetics} &= \underbrace{n_\mathrm{e}\sum_{k<i} n_k C_{ki} - n_\mathrm{e} n_\mathrm{i}\sum_{j>i} C_{ij} - n_\mathrm{i} n_\mathrm{e}\sum_{j>i} F_{ij} + n_\mathrm{e}\sum_{j>i} n_j F_{ji}}_{\text{electron-impact de/excitation}} \\ &\quad \underbrace{\times n_1\sum_{k<i} n_k K_{ki} - n_1 n_\mathrm{i}\sum_{j>i} K_{ij} - n_\mathrm{i} n_1\sum_{j>i} L_{ij} + n_1\sum_{j>i} n_j L_{ji}}_{\text{atom-impact de/excitation}} \\ &\quad \underbrace{-n_\mathrm{i} n_\mathrm{e} S_\mathrm{i} + n_{\mathrm{Ar}_+} n_\mathrm{e}^2 Q_\mathrm{i}}_{\text{electron-impact ionization / 3-body recomb.}} \underbrace{-n_\mathrm{i} n_1 V_\mathrm{i} + n_{\mathrm{Ar}_+} n_\mathrm{e} n_1 W_\mathrm{i} - \sum_{j=2}^{5} c_j K^I_{ij} n_j n_\mathrm{i}}_{\text{atom-impact ionization / 3-body recomb.}} \\ &\quad \underbrace{+n_{\mathrm{Ar}_+} n_\mathrm{e}\Lambda_\mathrm{i} R_\mathrm{i}}_{\text{radiative recomb.}} \underbrace{+\sum_{j>i}\eta_{ji} A_{ji} n_j - n_\mathrm{i}\sum_{k<i}\eta_{ik} A_{ik}}_{\text{radiative emission}} \underbrace{+S^m_\mathrm{i}}_{Ar_2{}^+ \text{ and } Ar_2{}^* \text{ processes}}\end{aligned} \tag{16}$$

$$\begin{aligned}\dot{\omega}_e \equiv \left.\frac{\partial n_\mathrm{e}}{\partial t}\right|_\mathrm{kinetics} &= n_\mathrm{e}\sum_i S_\mathrm{i} n_\mathrm{i} - n_{\mathrm{Ar}_+} n_\mathrm{e}^2\sum_i Q_\mathrm{i} + n_1\sum_i V_\mathrm{i} n_\mathrm{i} - n_{\mathrm{Ar}_+} n_\mathrm{e} n_1\sum_i W_\mathrm{i} \\ &\quad + \sum_{i=2}^{5}\sum_{j=i}^{5} K^I_{ij} n_j n_\mathrm{i} - n_{\mathrm{Ar}_+} n_\mathrm{e}\sum_i \Lambda_\mathrm{i} R_\mathrm{i} + S^m_\mathrm{e}.\end{aligned} \tag{17}$$

The expression for the net production rate of atomic ions is identical to that of electrons (equation (17)), except for additional contributions from $Ar_2{}^+$ and $Ar_2{}^*$ processes. Finally, the net production rate of electron energy, $\dot{\omega}_{e_\mathrm{e}}$, which appears in equation (4), can be expressed as shown in equation (18), where $Z^2_\mathrm{eff} = 1.67$ is an effective charge (Kapper and Cambier 2011), $\overline{g} = 1$ is the gaunt factor, c is the speed of light constant, and m_Ar is the mass of the argon atom. The rates k_en and k_ei for electron–neutral and electron–ion (Coulomb) elastic collisions, respectively, are evaluated as done by Kapper and Cambier (2011). The Bremsstrahlung

[6] The lowest energy electronic configuration of single-ionized argon (Ar II) is [Ne] 3 s^2 3 p^5. The unpaired electron results in two spin-split levels with total orbital angular momentum quantum numbers, j_c, of 1/2 and 3/2. Thus, there are two ionization limits (Bogaerts *et al* 1998).

[7] The subscript α, as appears in equation (1), denotes different species, while the subscript *i* refers to the atomic energy levels of argon excited states.

radiation term is included in equation (18) for completeness, though its contribution is expected to be negligible compared to other terms under the conditions studied. The term $S^m_{e_e}$ represents the contributions from processes involving the $Ar_2{}^+$ and $Ar_2{}^*$ species.

$$\dot{\omega}_{e_e} \equiv \frac{\partial}{\partial t}\left(\frac{3}{2}k_B n_e T_e\right)\bigg|_{\text{kinetics}} = n_e \sum_i \sum_{j>i} \varepsilon_{ij}\left(n_j F_{ji} - n_i C_{ij}\right) + n_e \sum_i \varepsilon_{Ii}\left(n_e n_{Ar_+} Q_i - n_i S_i\right)$$
$$- n_e n_{Ar_+} \sum_i \Lambda_i R'_i \underbrace{-n_{Ar_+} n_e \frac{16\pi^2}{3\sqrt{3}} \frac{\overline{\nu_e} Z^2_{\text{eff}} q_e{}^6 \overline{g}}{m_e h \left(4\pi\epsilon_0 c\right)^3}}_{\text{Bremsstrahlung}}$$
$$\times \underbrace{+3n_e n_b k_B\left(T_g - T_e\right)\frac{m_e}{m_{Ar}} k_{en} + 3n_e n_{Ar_+} k_B\left(T_g - T_e\right)\frac{m_e}{m_{Ar}} k_{ei}}_{\text{Elastic}} + S^m_{e_e}. \tag{18}$$

The rate coefficients for atom and electron collision processes are calculated from the corresponding collision cross-sections, by integrating them over the relevant energy distribution function $f(\epsilon)$. For electron-impact processes, the EEDF is evaluated as described in section 2.2. For atom-impact processes, a Maxwellian distribution at temperature T_g is assumed. In particular, the rate coefficients are evaluated as shown in equation (19), where $\sigma(\epsilon)$ is the collision cross-section for the relevant process, $v(\epsilon) = \sqrt{\frac{2\epsilon}{\mu}}$ represents a collision velocity at energy ϵ, with μ denoting the reduced mass of the colliding particles (either m_e for electron-impact processes or $m_{Ar}/2$ for atom-impact processes), and ε_t is the threshold energy for the process. Additionally, the rate coefficients for radiative recombination, as used in equation (18), are calculated from the first moment of the EEDF with respect to energy, see equation (20).

$$R = \int_{\varepsilon_t}^{\infty} f(\epsilon)\,\sigma(\epsilon)\,v(\epsilon)\,\mathrm{d}\epsilon, \tag{19}$$

$$R' = \int_0^{\infty} \epsilon f(\epsilon)\,\sigma(\epsilon)\,v(\epsilon)\,\mathrm{d}\epsilon. \tag{20}$$

Fine-structure electron-impact excitation cross-sections, $\sigma^e_{ij}(\epsilon)$, (process I.) are obtained from the LXCat database (https://nl.lxcat.net/home/ accessed in January 2023). Specifically, the B-spline R-matrix (BSR) data by Zatsarinny (2006) have been employed in this study. The BSR data are the most complete collection and are known to be accurate for near-neutral systems (Chung *et al* 2021). Information on the cross-section for electron-impact ionization (process II.) from the ground state is also sourced from the BSR data. For electron-impact ionization from excited states, the cross-sections are determined using the semi-classical formulation by Deutsch *et al* (2004), see equations (21) and (22), where r_{nl} represents the radius of the outermost valence electron (characterized by the quantum numbers n and l), ξ_{nl} denotes the number of electrons in that sub-shell (unity in this case), g_{nl} are weighting factors, and a, b, c, and d are model constants. For the values of these parameters, we refer to the work of Deutsch *et al* (2004).

$$\sigma^e_i(\epsilon) = g_{nl}\pi r^2_{nl}\xi_{nl} f_i(\epsilon), \tag{21}$$

$$f_i(\epsilon) = d\frac{\varepsilon_{Ii}}{\epsilon}\left(\frac{\frac{\epsilon}{\varepsilon_{Ii}} - 1}{\frac{\epsilon}{\varepsilon_{Ii}} + 1}\right)^{\alpha}\left[b + c\left(1 - \frac{\varepsilon_{Ii}}{2\epsilon}\right)\right.$$
$$\left.\times \ln\left(2.7 + \left(\epsilon/\varepsilon_{Ii} - 1\right)^{1/2}\right)\right], \tag{22}$$

Bound-bound radiative transitions are also incorporated into the model (process III.). The Einstein coefficients for spontaneous emission, A_{ji}, are obtained from the NIST atomic spectra database (https://physics.nist.gov/PhysRefData/ASD/levels_form.html accessed in January 2023). Data for certain transitions not available in the NIST database are sourced from BSR calculations by Zatsarinny and Bartschat (2006). *A priori* calculations for the plasma conditions considered in this study indicate that resonance transitions (those to the ground state) are optically thick or in an intermediate regime. A comprehensive treatment of radiation would require the solution of the radiative transfer equation. However, a widely adopted approach to circumvent such complex calculations is based on the application of escape factors (Golubovskii *et al* 2013). Escape factors, η_{ji}, were applied to all radiative transitions in the model. These were obtained from equation (8) of Chai and Kwon (2019), which accounts for radiation trapping in a finite cylindrical geometry (Golubovskii *et al* 2013) with Doppler broadening. The geometric parameters used in the evaluation correspond to the electrode radius and inter-electrode gap of the glow discharge device.

Cross-sections for atom-impact collisional processes (process IV.) are typically based on hydrogenic approximations. We have employed Drawin's formula (Drawin and Emard 1973) to describe atom-impact excitation cross-sections for optically allowed transitions (Vlcek 1989) see equation (23),

where α_0 represents the first Bohr radius, $\varepsilon_{\mathrm{I_H}}$ denotes the ionization energy of atomic hydrogen, m_{H} is the mass of the hydrogen atom, ξ_{i} is the number of optical electrons (6 for the ground state and 1 for the excited states (Bultel *et al* 2002)), and f_{ij} is absorption oscillator strength of the transition, as obtained from the NIST atomic spectra database.

$$\sigma_{ij}^{\alpha}(\epsilon) = 4\pi\alpha_0^2\left(\frac{\varepsilon_{\mathrm{I_H}}}{\varepsilon_{ij}}\right)^2\frac{m_{\mathrm{Ar}}}{m_{\mathrm{H}}}\xi_{\mathrm{i}}^2 f_{ij}\frac{2m_{\mathrm{e}}}{m_{\mathrm{Ar}}+m_{\mathrm{e}}} \times \frac{\frac{\epsilon}{\varepsilon_{ij}}-1}{\left[1+\frac{2m_{\mathrm{e}}}{m_{\mathrm{Ar}}+m_{\mathrm{e}}}\left(\frac{\epsilon}{\varepsilon_{ij}}-1\right)\right]^2}, \tag{23}$$

Cross-sections for the atom-impact excitation processes between states in the 4 s manifold are described by equation (24) (Bultel *et al* 2002), where $\varepsilon_{ij\,[\mathrm{eV}]}$ is the transition energy in eV, and the β_{ij}^{*} constants are listed in table IV of Kapper and Cambier (2011). Interestingly, there are no available cross-sections for the remaining forbidden transitions.

$$\sigma_{ij}^{\alpha}(\epsilon) = \beta_{ij}^{*}\frac{\epsilon-\varepsilon_{ij}}{\varepsilon_{ij\,[\mathrm{eV}]}^{2.26}}, \tag{24}$$

The atom-impact ionization cross-section from the ground state (process V.(a)) is provided by equation (25) (Haugsjaa and Amme 1970), where $\sigma_1^{\alpha}(\epsilon)$ is in m^2, and $\epsilon_{[\mathrm{eV}]}$ denotes electron energy in eV.

$$\sigma_1^{\alpha}(\epsilon) = 1.8\cdot10^{-25}\left(\epsilon_{[\mathrm{eV}]}-15.76\right)^{1.3}, \tag{25}$$

For all other levels, Drawin's formula is applied to determine the ionization cross-sections (Drawin 1968), see equation (26).

$$\sigma_{\mathrm{i}}^{\alpha}(\epsilon) = 4\pi\alpha_0^2\left(\frac{\varepsilon_{\mathrm{I_H}}}{\varepsilon_{\mathrm{I}i}}\right)^2\frac{m_{\mathrm{Ar}}}{m_{\mathrm{H}}}\xi_{\mathrm{i}}^2\frac{2m_{\mathrm{e}}}{m_{\mathrm{Ar}}+m_{\mathrm{e}}} \times \frac{\frac{\epsilon}{\varepsilon_{\mathrm{I}i}}-1}{\left[1+\frac{2m_{\mathrm{e}}}{m_{\mathrm{Ar}}+m_{\mathrm{e}}}\left(\frac{\epsilon}{\varepsilon_{\mathrm{I}i}}-1\right)\right]^2}. \tag{26}$$

Collisions between excited states in the 4 s manifold can also lead to ionization (process V.(b)). Ionization rate coefficients for collisions between atoms in metastable, resonance, and metastable and resonance states are provided by equation (27) (Zhiglinsky 1994, Chai and Kwon 2019), where the rates are given in $\mathrm{m^3\,s{-}1}$.

$$K_{\mathrm{mm}}^{I} = 1.2\cdot10^{-15},\quad K_{\mathrm{rr}}^{I} = 1.14\cdot10^{-20}\sqrt{\frac{16\,k_{\mathrm{B}}\,T_{\mathrm{g}}}{\pi\,m_{\mathrm{Ar}}}},\quad K_{\mathrm{rm}}^{I} = 2.1\cdot10^{-15}, \tag{27}$$

Radiative recombination (process VI.) is treated based on cross-sections obtained for the reverse process of photoionization and the principle of detailed balance. The cross-sections for photoionization from the ground and excited states are given, respectively, by (Vlcek 1989, Bultel *et al* 2002):

$$\sigma_{v,1}(h\nu) = \begin{cases} 3.5\cdot10^{-21} & \varepsilon_{\mathrm{I}} \leqslant h\nu \leqslant 2\,\varepsilon_{\mathrm{I_H}} \\ 2.8\cdot10^{-20}\left(\frac{\varepsilon_{\mathrm{I_H}}}{h\nu}\right)^3 & h\nu > 2\,\varepsilon_{\mathrm{I_H}} \end{cases}, \tag{28}$$

$$\sigma_{v,i}(h\nu) = \gamma_{\mathrm{i}}\begin{cases} 2\cdot10^{-22} & \varepsilon_{\mathrm{I}i} \leqslant h\nu \leqslant 0.59\,\varepsilon_{\mathrm{I_H}} \\ 7.91\cdot10^{-22}\left(\frac{\varepsilon_{\mathrm{I}i}}{\varepsilon_{\mathrm{I_H}}}\right)^{\frac{5}{2}}\left(\frac{\varepsilon_{\mathrm{I_H}}}{h\nu}\right)^3 & h\nu \geqslant 0.59\,\varepsilon_{\mathrm{I_H}} \end{cases}, \tag{29}$$

where γ_{i} is 0.0763, 0.0458, 0.0305, and 0.0915 for $i = 2,3,4$, and 5, respectively (Vlcek 1989). Free-bound radiation is expected to be optically thin under the plasma conditions examined here. Therefore, the optical escape factors for free-bound transitions, Λ_{i}, are assumed to be unity.

Processes involving the argon molecular ion, Ar_2^+, (process VII.) are included in the analysis. These processes encompass atomic-to-molecular ion conversion, metastable–metastable associative ionization, dissociative recombination, and direct electronic dissociation. The corresponding rate coefficients are provided in equation (30), where T_{e} and T_{g} are expressed in Kelvin. For further details on these processes, we refer to Bultel *et al* (2002) and the references therein.

$$\begin{aligned} K_{\mathrm{MC}} &= 2.5\cdot10^{-43}\left(\frac{T_{\mathrm{g}}}{300}\right)^{-1.5}\ \mathrm{m^6\,s^{-1}}, \\ K_{\mathrm{MAI}} &= 6.3\cdot10^{-16}\left(\frac{T_{\mathrm{g}}}{300}\right)^{-0.5}\ \mathrm{m^3\,s^{-1}}, \\ K_{\mathrm{DR}} &= 8.5\cdot10^{-13}\left(\frac{T_{\mathrm{e}}}{300}\right)^{-0.67}\left(\frac{T_{\mathrm{g}}}{300}\right)^{-0.58}\ \mathrm{m^3\,s^{-1}}, \\ K_{\mathrm{DR}^*} &= 9.1\cdot10^{-13}\left(\frac{T_{\mathrm{e}}}{300}\right)^{-0.61}\left(\frac{T_{\mathrm{g}}}{300}\right)^{-0.58}\ \mathrm{m^3\,s^{-1}}, \\ K_{\mathrm{DD}} &= 1.36\cdot10^{-12}\exp\left\{\left[-\frac{24300+\left(\frac{2}{3}-j_{\mathrm{c}}\right)\cdot10^4}{T_{\mathrm{e}}}\right]\right\}\ \mathrm{m^3\,s{-}1} \end{aligned} \tag{30}$$

The rate coefficients for processes involving the excimer molecules, Ar_2^* (process VIII.), are provided in equation (31), where T_{e} and T_{g} are expressed in Kelvin. These coefficients are taken from Zhu and Pu (2010). In this study, we assume that the Ar_2 processes involve only the 4 s metastable states.

$$\begin{aligned} K_{\mathrm{MA}} &= 1.0\cdot10^{-44}\ \mathrm{m^6\,s^{-1}}, \\ K_{\mathrm{ED}} &= 1.0\cdot10^{-14}\exp\left\{\left(-\frac{11604.52}{T_{\mathrm{e}}}\right)\right\}\ \mathrm{m^3\,s^{-1}}, \\ K_{\mathrm{MMI}} &= 7.0\cdot10^{-16}\left(\frac{T_{\mathrm{g}}}{300}\right)^{0.5}\ \mathrm{m^3\,s^{-1}}, \\ K_{\mathrm{MI}} &= 7.0\cdot10^{-16}\left(\frac{T_{\mathrm{g}}}{300}\right)^{0.5}\ \mathrm{m^3\,s^{-1}}, \\ A_{\mathrm{Ar_2}^*} &= 10^6\ \mathrm{1\,s^{-1}} \end{aligned} \tag{31}$$

Cross-sections for the reverse of the processes discussed thus far are obtained by applying the principle of detailed balance (Mitchner and Kruger 1973, Oxenius 2012). Specifically,

collision cross-sections for de-excitation processes are evaluated from the corresponding excitation cross-sections based on the Klein-Rosseland relation:

$$\sigma_{\text{de-exct}}(j,i,\epsilon') = \frac{g_\text{i}}{g_j}\frac{\epsilon}{\epsilon'}\sigma_{\text{exct}}(i,j,\epsilon), \tag{32}$$

where $\epsilon' = \epsilon - \varepsilon_{ij}$ and g_i denotes the degeneracy of the $i-$th energy level. While similar relations for ionization and the corresponding three-body recombination processes can be derived for differential cross-sections (Oxenius 2012), it is not straightforward for the total cross-sections considered here, as cross-sections for three-body recombination processes depend on the bound energy of the third body. Assuming this energy is zero and utilizing the Saha relation, Bogaerts *et al* (1998) employed the following relation:

$$\sigma_{\text{3b-recomb}}(i,\epsilon') = \left(\frac{h^2}{2\pi m_\text{e} k T_\text{e}}\right)^{3/2}\frac{g_\text{i}}{2g_1^+}\frac{\epsilon}{\epsilon'}\sigma_{\text{ioniz}}(i,\epsilon), \tag{33}$$

where $\epsilon' = \epsilon - \varepsilon_{\text{I}i}$ and g_1^+ represents the degeneracy of the ion ground state. Finally, cross-sections for radiative recombination are derived from those for photoionization using the Milne relation in equation (34), where $\epsilon = h\nu - \varepsilon_{\text{I}i}$:

$$\sigma_{\text{rad.recomb}}(i,\epsilon) = \frac{g_\text{i}}{2g_1^+}\frac{(h\nu)^2}{m_\text{e}c^2}\frac{1}{\epsilon}\sigma_{\text{photoioniz}}(i,h\nu). \tag{34}$$

3. Numerical and computational details

One-dimensional simulations of a CCP RF glow discharge were performed. The RF CCP discharge device simulated in this study was recently developed at the University of Texas at Austin, a simplified schematic and a photograph of the discharge are provided in figure 2. The symmetrical device operates by generating a plasma discharge between two parallel plate electrodes driven by an external oscillating electric field with a frequency of $f = 13.56$ MHz. The uncoated aluminum electrodes are spaced $H = 2$ cm apart, each having a diameter of $D = 10$ cm. The discharge is enclosed by a Pyrex 7740 glass cylinder, which acts as the chamber's sidewall. More details on the experimental setup and results can be found in (O'Connor *et al* 2025).

The spatial discretization of Equations (1)–(5) is achieved using a Chebyshev-collocation method (Lin and Adomaitis 2001), ensuring high spatial accuracy in the computational domain. A fully implicit Crank–Nicolson method is employed for temporal integration because of its stability and second-order accuracy. The set of discretized nonlinear differential equations arising at each time step is solved using a Newton–Raphson method, with the Jacobian analytically evaluated for the fluid model and numerically evaluated for the CR model. This combination of spatial and temporal discretization techniques ensures accurate and stable numerical solutions for the glow discharge model.

The system of equations in this study yields time-periodic solutions due to the periodic boundary condition for the voltage at the powered electrode, as described in equation (9). This periodic forcing poses challenges, because more than 10^5 periodic cycles (Lymberopoulos and Economou 1993) are required to achieve excited state populations independent of initial conditions, due to their slow response time. Various efficient methods have been proposed to address this problem (Gogolides *et al* 1992, Lymberopoulos and Economou 1993). Here, we apply a shooting method, leveraging the sensitivity of the equations over one RF cycle to expedite the convergence to time-periodic solutions. Appendix B provides a detailed explanation of the algorithm.

The numerical implementation is executed using an in-house Python code tailored specifically for this study. Computations are performed on CPUs, with parallelization handled internally via NumPy. Each simulation begins with a transient phase, initialized with spatially uniform profiles, and runs for 125 or 256 RF cycles. Subsequently, a periodic steady-state solution is obtained using the shooting method described earlier, typically converging within approximately 12 iterations. Once a solution is established, this framework allows for parametric studies without requiring the full transient evolution to be repeated. The total execution time varies depending on the number of spatial grid points (N_p) and the number of excited states included in the CR model, ranging from several hours to a few days.

The code developed in this study has been released as open-source software at https://github.com/pecos/glowDischargeSolver/tree/cr-model-coupling. Additionally, the code includes an option to leverage GPU acceleration using CuPy and an option for time-step adaptivity for the transient phase. This implementation lays the groundwork for future extensions, including potential coupling with Boltzmann-equation solvers such as the one developed by Fernando *et al* (2024, 2025), which also leverages GPU acceleration.

Simulations were performed using the following parameters for prescribed pressures and electrode voltage amplitudes. The spatial discretization of the inter-electrode gap was carried out using $N_\text{p} = 150$ Chebyshev points, while the time step size for temporal discretization was set to $\Delta t \cdot f = 1/256$. Tests with $N_\text{p} = 300$ Chebyshev points showed that grid independence had been achieved, and the results are shown in appendix C. Unless otherwise stated, the SEE coefficient was $\gamma = 0.1$. A fixed electron temperature of $T_{\text{e,s}} = 0.5$ eV (Lymberopoulos and Economou 1993) was prescribed for the electron energy boundary condition, and the wall temperature was maintained at $T_{\text{g,w}} = 293.15$ K. The diffusion coefficient of the argon excited states was estimated from $n_\text{b} D_\alpha = 2.42 \cdot 10^{18}$ $\#/\text{cm s}^{-1}$ (Baranov *et al* 1981, Lymberopoulos and Economou 1993). The thermal conductivity of the background species was set to $\kappa_\text{b} = 17.7 \cdot 10^{-3}$ $\text{W m}^{-1}\,\text{K}^{-1}$ at 300 K.

4. Results and discussion

In this section, simulation results are presented and analyzed. We begin by discussing the key characteristics of the glow discharge and the underlying discharge physics predicted by the model. Particular emphasis is then placed on the

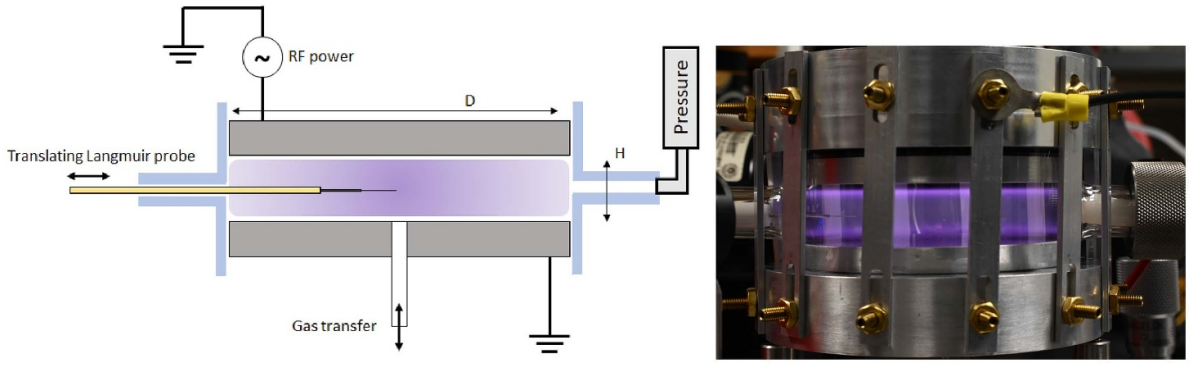

Figure 2. A simplified schematic (left) and a photograph (right) of the glow discharge device simulated in this study operating at a pressure of $P = 1$ Torr and an electrode peak-to-peak voltage of $V_{pp} = 150$ V, with $D = 10$ cm and $H = 2$ cm. Adapted from O'Connor *et al* (2025).

comparison between numerical predictions and experimental data. Comparisons with both experimental measurements and PIC/Monte Carlo simulation data from Donko *et al* (2023) are also included. This is followed by a detailed discussion of the assumptions and limitations associated with fluid modeling. The impact of the chosen EEDF modeling approach is then examined, and finally, the influence of higher-lying excited states (those beyond the 4p manifold) on the discharge characteristics is explored.

Simulations were conducted for a glow discharge device operating at pressures P ranging from 0.5 to 5 Torr and electrode peak-to-peak voltages V_{pp} of 150 V and 300 V. The reference case is defined as $P = 1$ Torr and $V_{pp} = 150$ V. For the reference case, the EEDFs were evaluated using Bolsig+, as described in section 2.2, the SEE coefficient was $\gamma = 0.1$, and the electron temperature of the emitted electrons at the electrodes was $T_{e,s} = 0.5$ eV. The results in the following sections include the first 14 atomic energy levels of neutral argon (4 s and 4p manifolds), while section 4.5.2 incorporates the first 30 levels. All simulations were allowed to reach a time-periodic steady-state using the shooting method described in section 3. Results were subsequently extracted and averaged over a full RF cycle. Therefore, all figures in this section present cycle-averaged quantities.

4.1. Glow discharge characteristics

The plasma discharge between the electrodes is sustained by the applied oscillating electric field. Ions and electrons are predominantly generated through electron-impact processes, while their primary loss mechanisms involve transport and diffusion to the walls. Upon reaching the walls, electrons are absorbed, and ions are neutralized, leading to their removal from the plasma. The difference in mobility between electrons and ions leads to the formation of positive space charge sheaths near the electrodes. The sheaths are regions of non-neutral plasma where the ion density is significantly higher than the electron density. The slower-moving ions accumulate in these regions, generating a net positive charge near the electrodes. For the reference case of $P = 1$ Torr and $V_{pp} = 150$ V, the model predicts a sheath thickness of approximately 1.8 mm on each side of the discharge, which together accounts for 18 % of the total inter-electrode spacing.

The predicted electric field and electric potential along the electrode-normal direction for the reference case of $P = 1$ Torr and $V_{pp} = 150$ V are presented in figure 3(a). The cycle-averaged potential of both the powered and the grounded electrode is zero, while the plasma potential remains positive relative to the electrodes. Within the sheaths, the electric field exhibits an approximately linear dependence on the position x, while the potential varies parabolically (Raizer *et al* 1995). On average, the electric field is negative near the left-hand-side electrode and positive near the right-hand-side electrode. This results in the acceleration of ions toward the electrodes, while the corresponding repulsive forces prevent electrons from readily reaching the surface, thereby maintaining the plasma discharge.

The number densities of electrons (e^-) and ions (Ar^+ and $Ar_2{}^+$) are illustrated in figure 3(b). It is evident that the plasma is electrically neutral in the central region, where the estimated Debye radius ($\lambda_D \approx 0.0677$ mm) is significantly smaller than the electrode spacing. However, near the electrodes, the ion density is significantly higher than the electron density. For the reference case, the number density of molecular ions, $Ar_2{}^+$, is only 2.5% of that of atomic ions, Ar^+. The density of argon excimer molecules, $Ar_2{}^*$, is even lower.

Figure 3(c) presents the electron temperature profile. Within the bulk plasma, the electron temperature remains relatively uniform but increases significantly in the sheath regions due to the strong electric fields. Specifically, the model predicts an electron temperature of 2.92 eV at the center of the discharge, whereas the heavy-species temperature remains near 300 K. It should be noted that the electron temperature is highly sensitive to the approach used for modeling the EEDFs. In the results presented here, EEDFs were determined using Bolsig+, as detailed in section 2.2. However, simulations that assumed Maxwellian EEDFs (see figure 7 to be discussed in section 4.5.1) predicted lower electron temperatures, with values around 1.24 eV at the center of the discharge.

Figure 3(d) presents the spatial distribution of the first argon metastable excited state ($1s5$ in Paschen notation) under the

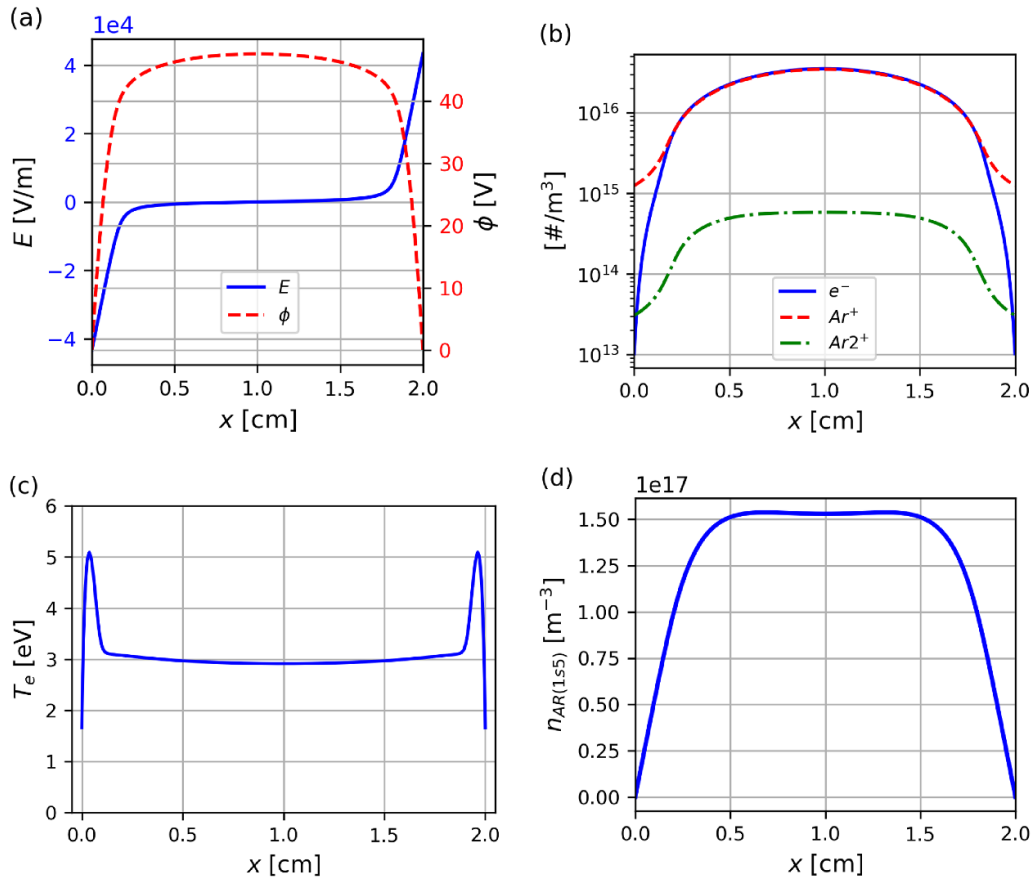

Figure 3. Glow discharge characteristics along the direction normal to the electrodes: (a) electric field E and potential ϕ, (b) electron and ion number densities, (c) electron temperature T_e, and (d) number density of the first argon metastable excited state (Paschen notation: $1s5$). Operating conditions of the glow discharge were $P = 1$ Torr and $V_{pp} = 150$ V.

reference operating conditions. This state is the most populated among all excited states and has a long lifetime, as the radiative transition to the ground state from this state is forbidden. The profile exhibits a weak double-peak structure, remaining nearly constant at the discharge center, with a slight rise near the sheath edges before dropping sharply at the electrodes.

4.2. Simulation results and comparison with experimental data from UT Austin

This section presents a comparison between numerical predictions and experimental data for excited states in the 4 s manifold (Paschen notation: $1s5 - 1s2$), excited states in the 4p manifold (Paschen notation: $2p10 - 2p1$), and the electron number density. Simulation results under various operating conditions are also presented in this section. Sources of discrepancies between simulation and experiment are discussed in section 4.4. The experimental data used for the comparison were collected from an RF CCP discharge device, shown in figure 2(right), which was recently developed at the University of Texas at Austin. The $1s5 - 1s2$ excited states were measured using LAS, while OES was used for the $2p10 - 2p1$ states. Both LAS and OES are line-of-sight diagnostic techniques. Electron number densities were determined using a Langmuir probe. A more detailed description of the discharge device and the OES measurements is given by O'Connor *et al* (2025). Details regarding the LAS measurements are discussed in appendix D. Additional details regarding the Langmuir probe measurements and their validity at the considered plasma conditions are given in appendix E.

The distribution of excited states at the center of the discharge for the reference case of $P = 1$ Torr and $V_{pp} = 150$ V is shown in figure 4(a). The number densities, n_i, have been divided by the degeneracies, g_i, of the respective energy levels, and the star symbol in the figure indicates the electron number density. Experimental uncertainties are only available for the $2p10 - 2p1$ excited states, while uncertainties associated with the electron number density measurements are expected to be large (see discussion in appendix E). Nevertheless, it is evident that the simulation systematically overestimates excited state populations and the electron number density compared to the experimental data. Specifically, the $1s5$ metastable state is overpredicted by a factor of 16, the $2p$ states by approximately a factor of 10, and the electron number density by a factor of 16. Figure 4(b) provides a magnified view of the excited state populations in the 4p manifold. The simulation predicts a distribution of excited states that resembles more a Boltzmann distribution, whereas the experimental data exhibit a clear deviation from thermal equilibrium.

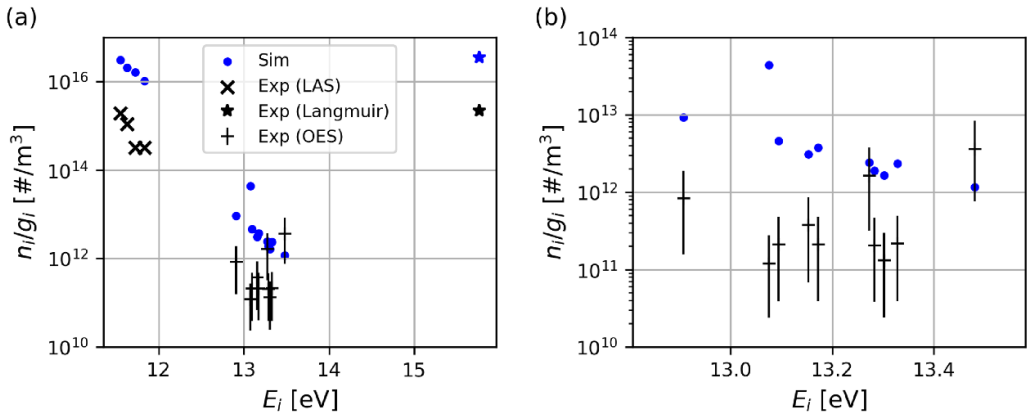

Figure 4. Comparison of numerical predictions with experimental data for the number densities of excited states at the center of the discharge: (a) distribution of excited states and (b) magnified view focusing on excited states within the 4p manifold (Paschen notation: $2p10 - 2p1$). The star symbol in (a) denotes electron number density. The LAS technique was used to measure the $1s5 - 1s2$ states, and OES was employed for the measurement of the $2p10 - 2p1$ states. Electron number densities were obtained using a Langmuir probe. Operating conditions of the glow discharge were $P = 1$ Torr and $V_{pp} = 150$ V. A logarithmic scale was used for the vertical axes.

Table 1. Simulation parameters used to generate the results presented in figure 5 and table 2. The table columns detail the operating conditions, the approach employed for modeling the EEDF, the secondary electron emission coefficient, the electron temperature of the emitted electrons at the electrodes, the number of Chebyshev points, and the time step size.

Case	P [Torr]	V_{pp} [V]	EEDF	γ	$T_{e,s}$ [eV]	N_p	$\Delta t \cdot f$
a	0.5	150	Druyvesteyn	0.1	0.5	150	1/256
b	0.5	300	Druyvesteyn	0.12	0.5	150	1/256
c	1	150	Druyvesteyn	0.1	0.5	150	1/256
d	1	300	Druyvesteyn	0.25	0.5	150	1/256
e	5	150	Maxwellian	0.5	1.0	300	1/512
f	5	300	Maxwellian	0.5	1.0	300	1/512

OES experimental data are available for several additional operating conditions: (*a*) $P = 0.5$ Torr, $V_{pp} = 150$ V; (*b*) $P = 0.5$ Torr, $V_{pp} = 300$ V; (*c*) $P = 1$ Torr, $V_{pp} = 150$ V; (*d*) $P = 1$ Torr, $V_{pp} = 300$ V; (*e*) $P = 5$ Torr, $V_{pp} = 150$ V; and (*f*) $P = 5$ Torr, $V_{pp} = 300$ V. Simulations corresponding to these conditions were performed, and the parameters used for each case are detailed in table 1.

Figure 5 compares numerical predictions with experimental data for the number densities of excited states within the 4p manifold ($2p10 - 2p1$) at the center of the discharge under the six different operating conditions detailed in table 1. The results show that the simulations consistently overpredict the experimental data by approximately a factor of 10 across all operating conditions. Nevertheless, the simulations capture the expected trend (O'Connor *et al* 2025) of higher number densities at increased applied voltages. Specifically, when the pressure is constant and the voltage is increased, the number densities of the excited states in the 4p manifold increase as anticipated. However, this increase is more pronounced in the simulations than in the corresponding experimental data.

Table 2 presents simulation results at the center of the discharge obtained for the operating conditions specified in table 1, including the electron number density n_e, the ratio of argon molecular to atomic ion number densities $n_{Ar_2^+}/n_{Ar^+}$, the number density of excimer molecules $n_{Ar_2^*}$, the number density of the $1s5$ metastable state n_{1s5}, the number density of the $1s4$ resonance state n_{1s4}, the escape factor η_{31} for the $1s4$ to ground state radiative transition, and the gas temperature T_g of the heavy species. The ratio $n_{Ar_2^+}/n_{Ar^+}$ varies between 0.5% and 8.3%, consistent with the findings of Bogaerts and Gijbels (1999). The data in the table show several notable trends. The electron number density n_e increases with increasing pressure. The ratio $n_{Ar_2^+}/n_{Ar^+}$, exhibits a more complex behavior, and for the higher pressure cases, this ratio decreases significantly when the applied electrode voltage increases from 150 to 300 V. Interestingly, the values of n_{1s5} at the center of the discharge remain relatively constant across the examined operating conditions, showing limited sensitivity to these parameters. In contrast, n_{1s4} exhibits some variation with the applied voltage. The radiative transition from the $1s4$ state to the ground state is optically thick, and the escape factor η_{31} decreases with increasing pressure, consistent with the observations of Wen *et al* (2023) at lower pressures. Moreover, $n_{Ar_2^*}$ increases with pressure but remains significantly lower than that of the metastables. The gas temperature, T_g, increases with pressure and applied voltage as expected.

4.3. Comparison with experimental and simulation data of Donkó et al (2023)

To further evaluate the predictive capability of the CR-fluid model, we simulated conditions corresponding to a recent study by Donko *et al* (2023), which included both experimental measurements and hybrid PIC/Monte Carlo simulation data for low-temperature argon glow discharges. Two operating conditions from Donko *et al* (2023) were considered in the present work: (a) $P = 50$ Pa, $V_{pp} = 150$ V and (b) $P = 150$ Pa, $V_{pp} = 150$ V. In these simulations, the inter-electrode spacing was set to $H = 3$ cm and the SEE coefficient was $\gamma = 0.07$, consistent with the referenced study.

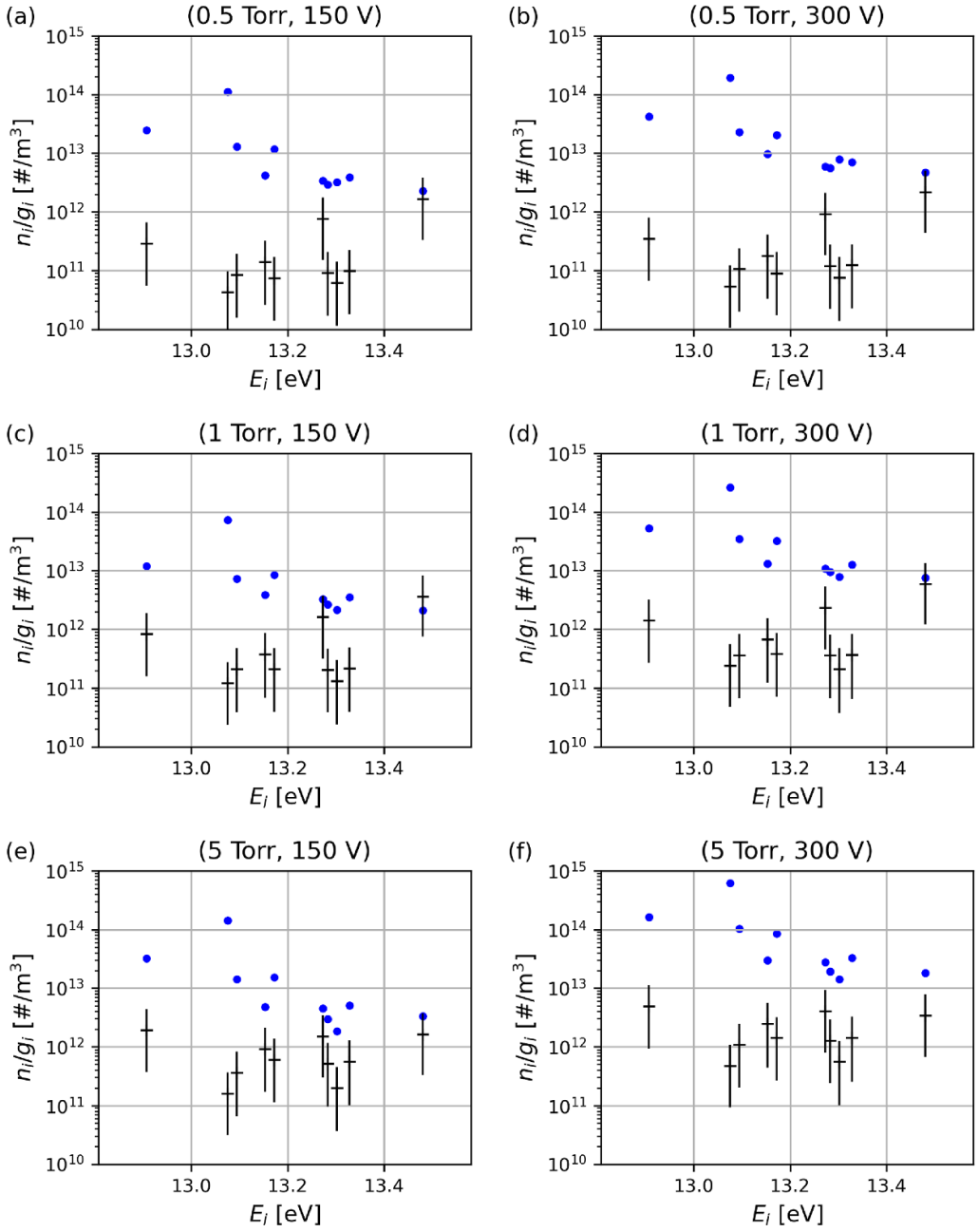

Figure 5. Comparison of numerical predictions with experimental data for the number densities of excited states within the 4p manifold (Paschen notation: $2p10 - 2p1$) at the center of the discharge under various operating conditions: (a) $P = 0.5$ Torr and $V_{pp} = 150$ V, (b) $P = 0.5$ Torr and $V_{pp} = 300$ V, (c) $P = 1$ Torr and $V_{pp} = 150$ V, (*d*) $P = 1$ Torr and $V_{pp} = 300$ V, (e) $P = 5$ Torr and $V_{pp} = 150$ V, and (f) $P = 5$ Torr and $V_{pp} = 300$ V. Measurements of the $2p10 - 2p1$ states (cross symbols) were obtained using OES, and experimental uncertainties are indicated in the figures. The simulation parameters used for each case are provided in table 1. A logarithmic scale is applied to the vertical axes.

Figure 6 shows the resulting spatial profiles of the $1s5$ metastable number density along the direction normal to the electrodes. In both cases, the fluid model developed in this study overpredicted the experimental data by roughly a factor of three at the discharge center. Potential sources of discrepancies between simulations and measurements, as well as limitations of the fluid modeling approach, are discussed in section 4.4. Importantly, the CR-fluid model shows good quantitative agreement with the PIC/Monte Carlo simulations reported by Donko *et al* (2023), particularly for the lower-pressure case ($P = 50$ Pa) as shown in figure 6(a). The PIC/Monte Carlo simulations appear to be better able to capture qualitative features of the number density profiles at the lower-pressure case ($P = 50$ Pa), i.e. the double-peak profile, and have improved quantitative agreement with the experimental data for the higher-pressure case ($P = 150$ Pa),

Table 2. Simulation results at the center of the discharge for the cases listed in table 1. The columns provide the electron number density, the ratio of the number densities of argon molecular to atomic ions, the number density of the argon excimer molecules, the $1s5$ metastable state number density, the $1s4$ resonance state number density, the escape factor η_{31} for the $1s4$ to ground state radiative transition, and the gas temperature T_g.

Case	n_e [$\#/m^3$]	$n_{Ar_2^+}/n_{Ar^+}$ [%]	$n_{Ar_2^*}$ [$\#/m^3$]	n_{1s5} [$\#/m^3$]	n_{1s4} [$\#/m^3$]	η_{31} [-]	T_g [K]
a	$4.51 \cdot 10^{16}$	1.82	$2.15 \cdot 10^{12}$	$1.79 \cdot 10^{17}$	$8.45 \cdot 10^{16}$	$2.03 \cdot 10^{-5}$	299
b	$4.32 \cdot 10^{16}$	2.41	$8.30 \cdot 10^{11}$	$2.76 \cdot 10^{17}$	$1.36 \cdot 10^{17}$	$2.04 \cdot 10^{-5}$	300
c	$4.47 \cdot 10^{16}$	1.93	$2.21 \cdot 10^{12}$	$1.88 \cdot 10^{17}$	$8.16 \cdot 10^{16}$	$9.74 \cdot 10^{-6}$	299
d	$1.24 \cdot 10^{17}$	0.50	$2.41 \cdot 10^{12}$	$2.14 \cdot 10^{17}$	$1.02 \cdot 10^{17}$	$1.02 \cdot 10^{-5}$	308
e	$1.28 \cdot 10^{17}$	8.30	$6.36 \cdot 10^{13}$	$2.46 \cdot 10^{17}$	$9.60 \cdot 10^{16}$	$1.99 \cdot 10^{-6}$	319
f	$8.20 \cdot 10^{17}$	0.74	$4.65 \cdot 10^{13}$	$2.52 \cdot 10^{17}$	$1.26 \cdot 10^{17}$	$2.62 \cdot 10^{-6}$	380

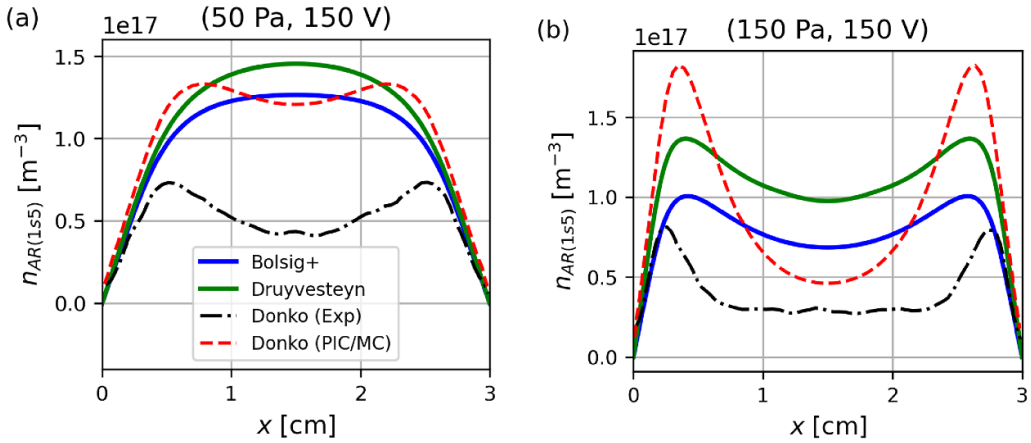

Figure 6. Comparison of numerical predictions for the first argon metastable excited state (Paschen notation: $1s5$) with experimental and simulation (PIC/Monte Carlo) data from Donko *et al* (2023): (*a*) $P = 50$ Pa and $V_{pp} = 150$ V, (*b*) $P = 150$ Pa and $V_{pp} = 150$ V. Simulation results using Bolsig+-derived and Druyvesteyn EEDFs are also compared. The inter-electrode spacing was $H = 3$ cm and the secondary electron emission coefficient was $\gamma = 0.07$. The results are plotted along the direction normal to the electrodes..

in particular at the center of the discharge. Possible sources of the observed differences between the CR-fluid and PIC/Monte Carlo models include variations in the extensive input data sets, differences in the predicted EEDFs, and the treatment of electron and ion transport.

To examine the sensitivity of the results to the choice of EEDF, additional simulations were performed using a Druyvesteyn distribution and are compared with those using a Bolsig+-derived EEDF. The Bolsig+-derived EEDF predicts lower metastable number densities and shows improved agreement with experimental data, in particular at the higher pressure condition ($P = 150$ Pa). These findings underscore the importance of accurate EEDF modeling in capturing key discharge features such as metastable state distributions.

4.4. Discussion of fluid modeling assumptions and limitations

The preceding discussion highlights that the CR-fluid model systematically overpredicts both excited-state populations and electron number density compared to experimental data. While the agreement with the experimental measurements reported by Donko *et al* (2023) is somewhat better than with the UT Austin data, and even closer to the PIC/Monte Carlo simulations from the same study, the model still overestimates experimental values in both discharge setups.

Given the complexity of plasma dynamics, discrepancies between simulations and experimental data are not unexpected. At this time, it is not possible to definitively pinpoint the causes of the discrepancies observed in figures 4–6. However, some insights can be gained by examining potential sources of uncertainty and limitations inherent to the current model. The modeling errors that arise from the relatively simplistic treatment of the EEDF in this study are discussed in more detail in section 4.5.1.

As discussed in section 2.1, we employed a 1D approximation based on the fact that the electrode diameter is five times larger than the inter-electrode spacing. While this approximation simplifies the analysis, it is important to note that 2D effects might play a significant role in the actual plasma behavior. For instance, electron and ion losses at the sidewalls of the chamber are not captured by the current 1D model. In addition to this, both LAS and OES are line-of-sight diagnostic techniques that yield averaged values of radially varying number densities. These factors may contribute to some of the observed discrepancies between the simulation and experimental results.

Ions drift slowly through the bulk plasma but rapidly accelerate toward the electrodes once they enter the sheath regions, where they are neutralized upon impact. The results of the present study were found to be sensitive to the ion mobility data. Specifically, a comparison between simulations using a constant ion mobility from Lymberopoulos and Economou (1993) and those using a variable ion mobility, as expressed in equation (13), revealed a difference of approximately 60% in the predicted number density of the 1*s*5 metastable state. This finding is consistent with the observations of Gogolides and Sawin (1992), suggesting that ion transport plays a critical role in the overall discharge dynamics. In our model, ion transport was described using the drift-diffusion approximation, which is typically more justified for electrons, given their much smaller mass compared to background species and their rapid response to external electric fields. However, this approximation may be less valid for ions, as discussed by Gogolides and Sawin (1992).

Additionally, ions can gain significant energy in the strong electric fields of the sheaths, which increases their temperature, as shown by Wen *et al* (2021). This increase in ion temperature affects the ion diffusion coefficient, which rises linearly with temperature according to equation (14). However, our model assumes thermal equilibrium between ions and background gas, potentially underestimating ion diffusional losses to the electrodes. Furthermore, some researchers (Bogaerts and Gijbels 1999) developed a hybrid model that treats fast argon ions and atoms in the RF sheaths using a Monte Carlo approach. Recently, Donko *et al* (2023) used a 1D PIC/Monte Carlo method to describe ion and electron dynamics, achieving improved agreement between predicted and measured values for the 1s5 metastable states, as discussed in section 4.3. While it is unclear whether such methods would introduce significant improvements in the present study, the simplified treatment of ion transport and sheath dynamics in this work could contribute to the discrepancies observed between the numerical predictions and experimental data.

Modeling errors may also stem from the relatively simple treatment of radiation employed in our study, which is based on escape factors (Chai and Kwon 2019). In contrast, Zhu *et al* (2015) developed a 2D CR model that accounted for the effective radiative relaxation rate using a modified Holstein–Biberman equation, exhibiting some differences to the escape-factor approach. However, their study focused on argon plasmas at much lower pressures (0.1–1 Pa). In our case, the resonance transitions are expected to be optically thicker, likely mitigating discrepancies between the two approaches.

Another source of uncertainty arises from the cross-sections used to model the processes described in section 2.3, particularly the electron-impact processes, which play a dominant role. The BSR dataset (Zatsarinny 2006) was employed in this study for electron-impact excitation. The BSR dataset is the most comprehensive, and its cross-sections tend to be lower than those from other available datasets (Chung *et al* 2021). Simulations using electron-impact excitation cross-sections from the Biagi dataset (Biagi 2011) were also explored but did not lead to significant differences. Additionally, there is uncertainty associated with the cross-sections for electron-impact ionization from excited states. Step-wise ionization is recognized as the dominant electron production mechanism (Lymberopoulos and Economou 1993, Donko *et al* 2023), and the cross-sections frequently used in the literature are based on semi-classical formulations, such as those provided by Deutsch *et al* (2004).

4.5. Investigation of model choices

4.5.1. Effect of EEDF modeling. The approach used to model the EEDF can significantly affect the simulation results, representing a potential source of error. The choice of EEDF modeling influences both the rates of electron-impact processes, as described by equation (19), and the coefficients for electron mobility and diffusion. For the reference case, EEDFs were evaluated using the Bolsig+ code, as detailed in section 2.2. It should be noted that this approach assumes a quasi-static EEDF and neglects time-dependent effects, which may become significant (Tejero-del Caz *et al* 2021) in the pressure range considered in this study.

Figure 7 compares simulations using Bolsig-derived, Druyvesteyn, and Maxwellian EEDFs for $P = 1$ Torr and $V_{pp} = 150$ V. figure 7(d) shows the EEDFs at the center of the discharge ($x = 1$ cm) computed using the three different approaches. The 'Bolsig+' case exhibits stronger depletion at higher electron energies under these discharge conditions. The simulation employing Maxwellian EEDFs predicted higher number densities—approximately by a factor of 2—for both excited states and electrons compared to the simulation employing Bolsig-derived EEDFs. Significant discrepancies are also observed among the three approaches in the plasma potential (figure 7(b)) and electron temperature (figure 7(c)). The 'Druyvesteyn' case predicted results that fall between the two curves representing the 'Bolsig+' and 'Maxwellian' cases. Specifically, the predicted plasma potential at the center of the discharge was 47.58 V for the 'Bolsig+' case, 43.78 V for the 'Druyvesteyn' case, and 38.58 V for the 'Maxwellian' case, while the experimental value, measured using a Langmuir probe, is 46.3 V, as summarized in table 3.

Although these differences are insufficient to explain the discrepancies between simulations and experimental data discussed in section 4.2, they underscore the need for a more accurate treatment of the EEDF. Alternative approaches, such as hybrid models incorporating PIC/Monte Carlo techniques (Donko *et al* 2023), direct solutions of the Boltzmann equation (Fernando *et al* 2025), and high-order moment closures for fluid models (Laguna *et al* 2023, Alvarez Laguna *et al* 2024) or advanced fluid models (Becker *et al* 2017), could enhance accuracy, albeit with increased computational demands.

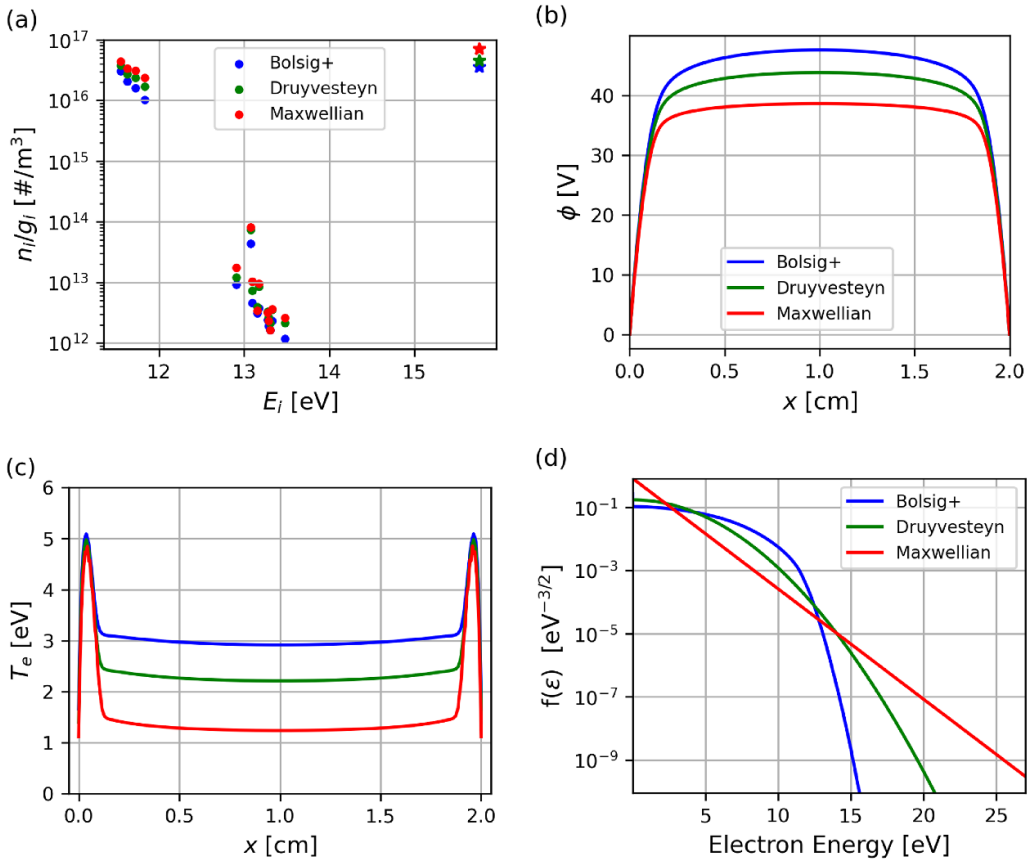

Figure 7. Comparison of numerical predictions using Bolsig-derived, Druyvesteyn, and Maxwellian EEDFs: (a) distribution of excited states, (b) electric potential, (c) electron temperature, and (d) EEDFs at the discharge center ($x = 1$ cm) computed as described in section 2.2. The star symbol denotes electron number density. Operating conditions of glow discharge were $P = 1$ Torr and $V_{pp} = 150$ V. A logarithmic scale was used for the vertical axis in (*a*).

Table 3. Comparison of numerical predictions with experimental data for the plasma potential ϕ at the center of the discharge. Results were obtained using Bolsig-derived, Druyvesteyn, and Maxwellian EEDFs. Operating conditions of glow discharge were $P = 1$ Torr and $V_{pp} = 150$ V.

Bolsig+	Druyvesteyn	Maxwellian	Experimental
47.58 V	43.78 V	38.58 V	46.3 V

4.5.2. Effect of higher-lying excited states. The results presented so far consider only the first 14 atomic energy levels of neutral argon, specifically the excited states in the 4 s and 4p manifolds. At this stage, it is worth exploring the impact of including higher-lying excited states on the discharge dynamics. Thus, a simulation incorporating the first 30 atomic energy levels, which includes the 4 s, 4p, 3d, and 5 s manifolds (up to 14.304 eV), was performed and compared to the base simulation. The results, shown in figure 8, compare the base case with 14 energy levels, labeled as '$Ns = 14$', to the case with higher-lying states, labeled as '$Ns = 30$', for reference conditions $P = 1$ Torr and $V_{pp} = 150$ V. For this condition, accounting for higher-lying excited states (beyond the 4p manifold) had a minimal effect on the discharge dynamics. Specifically, the '$Ns = 30$' case predicted a 6% decrease in the electron number density, a 14% increase in the number densities of the $2p10 - 2p1$ excited states, and a difference of less than 3% in the number densities of the $1s5 - 1s2$ excited states. This suggests that the population densities of the higher-lying states were too low to contribute significantly to the discharge dynamics. Therefore, the discrepancies between the simulation and experimental data discussed earlier in section 4.2 cannot be attributed to the influence of higher-lying excited states.

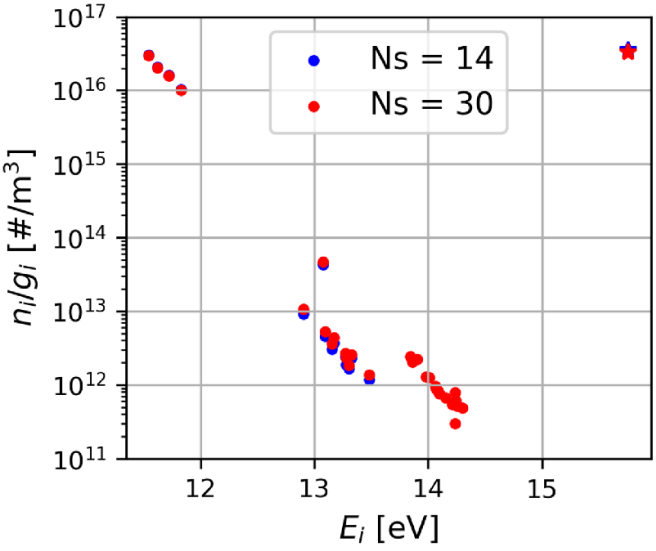

Figure 8. Comparison of numerical predictions incorporating 14 and 30 atomic energy levels of neutral argon: distribution of excited states. The star symbol denotes electron number density. Operating conditions of glow discharge were $P = 1$ Torr and $V_{pp} = 150$ V. A logarithmic scale was used for the vertical axis.

5. Conclusions

The objective of this study was to develop a comprehensive CR model and couple it with a 1D two-temperature fluid model to investigate capacitively coupled RF glow discharges in argon at intermediate pressures (∼1 Torr). The fluid model is formulated using the drift-diffusion approximation, while the CR model comprises a state-to-state approach and predicts the number densities of electrons, ions, individual excited states within the 4 s, 4p, 3d, and 5 s manifolds, atomic and molecular ions, and argon excimer molecules. The CR model accounts for a wide range of atomic processes, including electron-impact excitation and ionization, radiation emission, heavy-particle collisions, and processes involving Ar_2^+ and Ar_2^* molecules. Non-Maxwellian EEDFs, calculated using Bolsig+, are incorporated into the model, and fine-structure collisional cross-sections are obtained from the LXCat database.

Numerical predictions were compared with experimental data for the argon 4 s and 4p excited states, as well as electron number density. The experimental data were obtained from an RF CCP discharge device, recently developed at the University of Texas at Austin, using OES, LAS, and Langmuir probe diagnostics. The simulations overpredicted the experimental data by at least an order of magnitude. Additional comparisons were conducted with experimental and hybrid PIC/Monte Carlo simulation data reported by Donko *et al* (2023). While comparison with the Donkó *et al* experimental measurements showed modest improvement, and better alignment was observed with the PIC/Monte Carlo results, the model continued to systematically overestimate experimental values. By examining potential sources of uncertainty and limitations within the current methodology, several possible reasons for the discrepancy and model improvements were discussed. Specifically, inadequate treatment of ion transport and sheath dynamics, as well as 2D effects such as electron and ion losses at the chamber sidewalls, were identified as potential contributing factors to the discrepancies.

A comparative analysis was conducted using Bolsig-derived, Druyvesteyn, and Maxwellian EEDFs. The simulation results demonstrated that both electron temperature and plasma potential are highly sensitive to the assumptions made regarding the shape of the EEDF. These differences in predicted plasma characteristics underscore the need for a more accurate treatment of the EEDF in fluid modeling.

We also investigated the effect of higher-lying excited states on discharge dynamics. While the base model included the first 14 atomic energy levels (the 4 s and 4p manifolds), a second simulation incorporating the first 30 atomic energy levels (the 4 s, 4p, 3d, and 5 s manifolds) was performed and compared to the base case. The results indicated that including these higher-lying excited states had a minimal impact on the predicted plasma behavior. Additionally, the ratio of argon molecular to atomic ion number densities ranged from 0.5% to 8.3%, exhibiting a decrease as the applied electrode voltage increased for the higher pressure cases.

While the fluid model developed in this study effectively captures key characteristics of argon CCP glow discharges, it is evident that further research is necessary to achieve quantitative agreement with experimental data. More systematic comparisons between simulations and experimental measurements will help assess the validity and limitations of fluid models for low-temperature plasma discharges. Future work will focus on addressing the limitations of the 1D approximation and enhancing the EEDF and ion transport modeling in the sheaths.

Data availability statement

All data that support the findings of this study are included within the article (and any supplementary files).

Acknowledgments

This material is based upon work supported by the U. S. Department of Energy, National Nuclear Security Administration, under Award Number DE-NA0003969. The authors acknowledge the Texas Advanced Computing Center (TACC) at The University of Texas at Austin for providing computational resources that have contributed to the research results reported within this paper. URL: www.tacc.utexas.edu. M. T. would like to acknowledge the helpful suggestions of the anonymous reviewers, which helped improve the quality of this manuscript.

Appendix A. Treatment of the background species

Let ne_t denote the total energy per unit volume. To begin, we have assumed that the bulk motion of the fluid is negligible, such that there is no contribution from the kinetic energy associated with the bulk velocity. The total energy is governed by the following equation:

$$\frac{\partial ne_\mathrm{t}}{\partial t} = \underbrace{-\frac{\partial q}{\partial x}}_{\text{transport}} + \underbrace{\sum_\alpha q_\mathrm{e} z_\alpha F_\alpha E}_{\text{Joule heating}} + \underbrace{\dot{Q}_\mathrm{rad}}_{\text{Radiative heating}}, \tag{35}$$

where the heat flux q is given by

$$q = \frac{5}{2}k_\mathrm{B}T_\mathrm{e}F_\mathrm{e} - \kappa_\mathrm{e}\frac{\partial T_\mathrm{e}}{\partial x} + \sum_{\alpha\in h}\left\{\left(C_{\mathrm{p},\alpha}T_\mathrm{g} + \varepsilon_\alpha\right)F_\alpha - \kappa_\alpha\frac{\partial T_\mathrm{g}}{\partial x}\right\}, \tag{36}$$

where $C_{\mathrm{p},\alpha}$ represents the specific heat capacity at constant pressure for species α. For ideal monatomic and diatomic gases, $C_{\mathrm{p},\alpha}$ is evaluated as $\frac{5}{2}k_\mathrm{B}$ and $\frac{7}{2}k_\mathrm{B}$, respectively. ε_α denotes the internal energy of species α (i.e. energy not associated with thermal motion), and the radiative heating is modeled in $\dot{Q}_\mathrm{rad}$. The required thermal conductivity coefficients may be computed from the diffusivity as follows:

$$\kappa_\alpha = C_{\mathrm{p},\alpha}n_\alpha D_\alpha. \tag{37}$$

For a mixture of N_s species, $N_\mathrm{s}-1$ species densities are evolved according to equation (1). The density of the dominant background species (e.g. argon ground state), denoted n_b, is evolved according to:

$$\frac{\partial n_\mathrm{b}}{\partial t} = S, \tag{38}$$

where the field S is determined by imposing the constraint that the pressure remains constant. We assume constant pressure is maintained by adding or subtracting the background species. Assuming this mass is introduced at the local gas temperature, this also introduces a source term on the righthand side of the heavy species and total energy equations. This source term is given by $\frac{3}{2}Sk_\mathrm{B}T_\mathrm{g}$ (assuming only monatomic species). Then, to determine S, we may use the relationship between the total energy and the pressure. Specifically,

$$ne_\mathrm{t} = \frac{3}{2}p + \sum_\alpha n_\alpha\varepsilon_\alpha. \tag{39}$$

Thus, since the pressure is fixed,

$$\frac{\partial ne_\mathrm{t}}{\partial t} = \frac{3}{2}\frac{\partial p}{\partial t} + \sum_\alpha \frac{\partial n_\alpha}{\partial t}\varepsilon_\alpha = \sum_\alpha \frac{\partial n_\alpha}{\partial t}\varepsilon_\alpha. \tag{40}$$

Using the total energy equation (35), with the addition of the source term imposed by addition of the background species, this result imposes a constraint that determines S:

$$\sum_\alpha \frac{\partial n_\alpha}{\partial t}\varepsilon_\alpha = -\frac{\partial q}{\partial x} + \sum_\alpha q_\mathrm{e}z_\alpha F_\alpha E + \dot{Q}_\mathrm{rad} + \frac{3}{2}Sk_\mathrm{B}T_\mathrm{g}. \tag{41}$$

Thus,

$$S = \frac{\sum_\alpha \frac{\partial n_\alpha}{\partial t}\varepsilon_\alpha + \frac{\partial q}{\partial x} - \sum_\alpha q_\mathrm{e}z_\alpha F_\alpha E - \dot{Q}_\mathrm{rad}}{\frac{3}{2}k_\mathrm{B}T_\mathrm{g}}. \tag{42}$$

Thus, using the ideal gas law to determine T_g from the species densities and electron energy,

$$\frac{3}{2}k_\mathrm{B}T_\mathrm{g} = \frac{\frac{3}{2}p - n_\mathrm{e}e_\mathrm{e}}{\sum_{\alpha\in h}n_\alpha}, \tag{43}$$

S may be determined given the state and its spatial derivatives.

Appendix B. Time-periodic solver: shooting method

Consider $\mathbf{u}$ as the vector of unknowns within the system. A time-periodic state is achieved when the difference between the initial condition $\mathbf{u}^0$ and the solution $\mathbf{u}^N$ after one complete period (where N represents the number of time steps for a full cycle) is zero. The residual, which measures this difference, is defined as:

$$\mathbf{R}\left(\mathbf{u}^0\right) = \mathbf{u}^N\left(\mathbf{u}^0\right) - \mathbf{u}^0 \approx 0. \tag{44}$$

The objective is to find $\mathbf{u}^0$ such that the residual $\mathbf{R}(\mathbf{u}^0)$ is minimized, ideally to zero. This is achieved using the Newton–Raphson method, which iteratively refines the initial guess $\mathbf{u}^0$. The partial derivative of the residual function with respect to $\mathbf{u}^0$ is given by:

$$\frac{\partial \mathbf{R}}{\partial \mathbf{u}^0} = \frac{\partial \mathbf{u}^N}{\partial \mathbf{u}^0} - I. \tag{45}$$

During each iteration k, the Newton–Raphson method updates the initial guess $\mathbf{u}^0$ as follows:

$$\mathbf{u}^0_{(k+1)} = \mathbf{u}^0_{(k)} + \Delta\mathbf{u}^0_{(k)}, \tag{46}$$

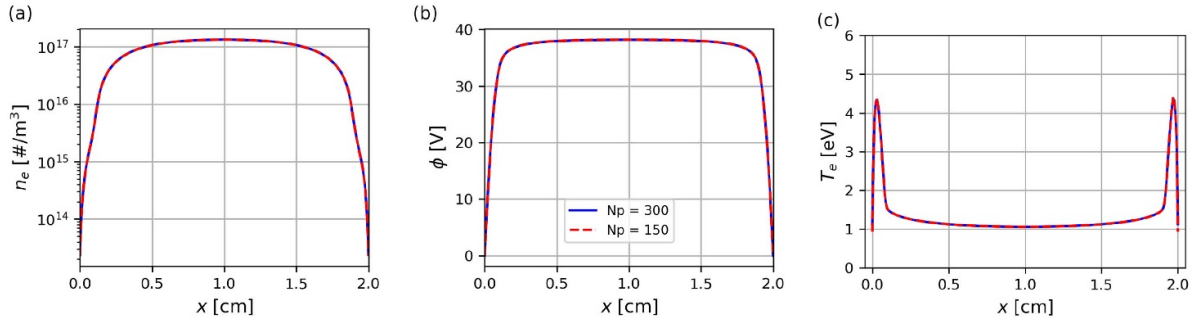

Figure 9. Grid independence study. Results were obtained using $N_p = 300$ and $N_p = 150$ Chebyshev points: (a) electron number density n_e, (b) electric potential ϕ, and (c) electron temperature T_e. Operating conditions of glow discharge were $P = 2.5$ Torr and $V_{pp} = 150$ V. A logarithmic scale was used for the vertical axis in (a).

where the correction term $\Delta\mathbf{u}^0$ at each iteration is determined by:

$$\Delta\mathbf{u}^0 = -\left[\frac{\partial\mathbf{R}}{\partial\mathbf{u}^0}\right]^{-1}\mathbf{R}\left(\mathbf{u}^0\right). \tag{47}$$

To evaluate $\frac{\partial\mathbf{u}^N}{\partial\mathbf{u}^0}$, we employ the Crank–Nicolson time discretization scheme, which is given by:

$$\frac{\mathbf{u}^{n+1}-\mathbf{u}^n}{\Delta t} = \frac{1}{2}\left[\mathbf{F}\left(\mathbf{u}^{n+1}\right)+\mathbf{F}\left(\mathbf{u}^n\right)\right], \tag{48}$$

where $\mathbf{F}$ is the function representing the system of differential equations. Differentiating this equation with respect to $\mathbf{u}^n$ gives:

$$\frac{1}{\Delta t}\left(\frac{\partial\mathbf{u}^{n+1}}{\partial\mathbf{u}^n}-I\right) = \frac{1}{2}\frac{\partial\mathbf{F}}{\partial\mathbf{u}}\bigg|_{n+1}\cdot\frac{\partial\mathbf{u}^{n+1}}{\partial\mathbf{u}^n}+\frac{1}{2}\frac{\partial\mathbf{F}}{\partial\mathbf{u}}\bigg|_{n}. \tag{49}$$

This can be rearranged to:

$$\left[I-\frac{\Delta t}{2}\frac{\partial\mathbf{F}}{\partial\mathbf{u}}\bigg|_{n+1}\right]\cdot\frac{\partial\mathbf{u}^{n+1}}{\partial\mathbf{u}^n} = I+\frac{\Delta t}{2}\frac{\partial\mathbf{F}}{\partial\mathbf{u}}\bigg|_{n}. \tag{50}$$

The algorithm proceeds as:

- Initialize the time step counter $n = 0$ and solve the linear system in equation (50) to obtain $A_1 = \frac{\partial\mathbf{u}^1}{\partial\mathbf{u}^0}$
- Set $A_0 = A_1$
- For $n = 1$, multiply both sides of equation (50) by A_0 and solve the linear system to update $A_1 = \frac{\partial\mathbf{u}^2}{\partial\mathbf{u}^0}$
- Repeat this process N times to compute $A_1 = \frac{\partial\mathbf{u}^N}{\partial\mathbf{u}^0}$, thus constructing the sensitivity matrix over the entire period.

This iterative approach continues until the initial conditions $\mathbf{u}^0$ converge to a time-periodic solution, defined as when the residual $\mathbf{R}(\mathbf{u}^0)$ is sufficiently close to zero within a specified tolerance.

Appendix C. Grid independence

A grid independence study was performed to verify that the spatial resolution does not influence the numerical results. The glow discharge model was simulated using $N_p = 300$ and $N_p = 150$ Chebyshev points across the inter-electrode gap. Figure 9 shows the electron number density n_e, electric potential ϕ, and electron temperature T_e for operating conditions of $P = 2.5$ Torr and $V_{pp} = 150$ V. The figure demonstrates that the two resolutions yield nearly identical results.

Appendix D. LAS measurements

Several atomic transitions were studied using tunable LAS to infer populations of argon 4*s* metastable and resonant states. The measurement is achieved by passing a widely tunable Titanium:Sapphire laser through the plasma volume and onto a photodetector. Some of the laser light is split and passed through an air-spaced etalon of known length and onto a second photodetector to provide a relative wavelength calibration from the resulting fringe pattern. As the laser wavelength is scanned across a transition, the absorption signal is measured and an absolute population density of the lower state in the transition can be obtained using:

$$\frac{\mathrm{d}P_\nu}{P_\nu} = -\left(n_i B_{ij}-n_j B_{ji}\right)h\nu\phi\left(\nu\right)\mathrm{d}z, \tag{51}$$

where P_ν is the laser power to the detector, B_{ij} and B_{ji} are the Einstein B-coefficients, ν is the laser frequency and z is in the direction of propagation of the laser beam.

If conditions are assumed to be uniform along the line of sight, the integration is over the plasma slab depth, taken to be the diameter of the discharge D, and gives the transmissivity $\tau(\nu)$:

$$\ln\left(\tau\left(\nu\right)\right) = -\left(n_i B_{ij}-n_j B_{ji}\right)h\nu\phi\left(\nu\right)D. \tag{52}$$

The population of the upper state in the transition is needed in this equation in order to correct for stimulated emission from the 4*p* states. The population density from the OES measurements is used to make this correction. The correction is very small ($<1\%$) for our experimental conditions. The resulting

population densities are reported in the appendix of O'Connor *et al* (2025).

Appendix E. Langmuir probe measurements

A Langmuir probe was used to measure the EEDF and the electron density via the moments of the EEDF. The basic concept of the diagnostic is to introduce a thin wire probe tip (1 mm in diameter) into the plasma volume and bias it relative to the plasma potential. The variation of electron current drawn by the probe as a function of the bias voltage can be related to the EEDF via the Druyvesteyn model (equation (53)) assuming 1) an isotropic EEDF and 2) that the electrons experience no collisions in the sheath around the probe tip. The probe incorporates RF and DC compensation electronics to minimize well-known perturbative effects of the probe measurement. These consist of self-resonant inductors tuned to the RF driving frequency and its harmonics as well as additional compensation electrodes which capacitively couple to the probe tip to reduce the sheath impedance. A DC reference probe tip is also used to account for local perturbations caused by the probe voltage sweep. The probe geometry is designed to taper down using several steps to contract from the 10 mm probe support to the 1 mm probe tip to minimize perturbations near the tip.

$$\frac{\mathrm{d}^2 I_\mathrm{e}}{\mathrm{d}V^2} = \frac{q_\mathrm{e}^2 A_\mathrm{p}}{4}\sqrt{\frac{2q_\mathrm{e}}{m_\mathrm{e}W}}F(W) \tag{53}$$

Here I_e is the electron current to the probe, V is the bias voltage, V_p is the plasma potential, A_p is the probe tip area, q_e is the electron charge, m_e is the electron mass, W is the electron kinetic energy and $F(W)$ is the EEDF. When the distribution function is found, the electron density can be found via equation (54).

$$n_\mathrm{e} = \int_0^\infty F(W)\,\mathrm{d}W \tag{54}$$

The presence of a second derivative operator on the measured current introduces the complication of noise amplification. We use a Savitzky–Golay filter to smooth and differentiate the probe trace. The plasma potential is found as the zero-crossing of the second derivative of the measurement. Measurement uncertainties were not computed for this technique and are expected to be large (only reliable for order of magnitude estimates of electron density). Worth noting, while the Druyvesteyn model is only strictly valid for the component of the measured current coming from electron flux (the measured current is the sum of contributions from both electrons and ions), the second derivative of the ion current is considered negligible and thus the second derivative of the measured current is considered equal to the second derivative of just the electron component (Godyak 1990, Godyak *et al* 2002, Godyak and Alexandrovich 2015).

Measurement at $P = 1$ Torr plasma condition was used for comparison with the model results. Based on estimates of the Debye length, probe sheath thickness, and electron mean free path, we estimate that the assumption of collisionless sheaths holds for $P \leqslant 1$ Torr in our discharge, but begins to break down at higher pressures.

ORCID iDs

Malamas Tsagkaridis 0000-0001-9649-9341
Todd A Oliver 0000-0001-9415-0429
Dan Fries 0000-0002-2951-3294
Ruairi O'Connor 0000-0001-5512-9627
Juan P Barberena-Valencia 0009-0002-7340-7365
Laxminarayan L Raja 0000-0002-5963-7183
Philip L Varghese 0000-0001-9796-0013
Robert D Moser 0000-0001-7735-1253

References

A Bogaerts and R Gijbels 1999 Monte Carlo model for the argon ions and fast argon atoms in a radio-frequency discharge *IEEE Trans. Plasma Sci.* **27** 1406–15

Akatsuka H 2019 Optical emission spectroscopic (OES) analysis for diagnostics of electron density and temperature in non-equilibrium argon plasma based on collisional-radiative model *Adv. Phys. X* **4** 1592707

Alves L 2014 The IST-LISBON database on LXCat *J. Phys.: Conf. Ser.* **565** 012007

Augustyniak E, Filimonov S and Borysow J 1999 Spatial distributions of absolute densities of argon metastable state $3^5_\mathrm{P}4\mathrm{S}$ in a gaseous electronics conference reference cell *J. Appl. Phys.* **86** 4767–71

Baranov I Y, Demidov V and Kolokolov N 1981 Temperature dependence of rate constants for metastable atomic-argon deactivation by slow electrons *Opt. Spectrosc.* **51** 316–8

Becker M M, Kählert H, Sun A, Bonitz M and Loffhagen D 2017 Advanced fluid modeling and pic/MCC simulations of low-pressure CCRF discharges *Plasma Sources Sci. Technol.* **26** 044001

Biagi S 2011 Biagi database (available at: www.lxcat.net/Biagi) (Accessed 28 May 2024)

Bogaerts A 1999 The glow discharge: an exciting plasma! *J. Anal. Atom. Spectrom.* **14** 1375–84

Bogaerts A and Gijbels R 1999 Role of Ar^2+ and Ar_2^+ ions in a direct current argon glow discharge: A numerical description *J. Appl. Phys.* **86** 4124–33

Bogaerts A, Gijbels R and Vlček J 1998 Collisional-radiative model for an argon glow discharge *J. Appl. Phys.* **84** 121–36

Bogaerts A, Gijbels R and WimGoedheer W 1999 Hybrid modeling of a capacitively coupled radio frequency glow discharge in argon: combined Monte Carlo and fluid model *Jpn. J. Appl. Phys.* **38** 4404–15

Bultel A, van Ootegem B, Bourdon A and Vervisch P 2002 Influence of Ar_2^+ in an argon collisional-radiative model *Phys. Rev. E* **65** 046406

Caz A T-del, Guerra V, Pinhão N, Pintassilgo C D and Alves L L 2021 On the quasi-stationary approach to solve the electron Boltzmann equation in pulsed plasmas *Plasma Sources Sci. Technol.* **30** 065008

Chai K-B and Kwon D-H 2019 Optical emission spectroscopy and collisional-radiative modeling for low temperature Ar plasmas *J. Quant. Spectrosc. Radiat. Transfer* **227** 136–44

Chen F F 2012 Lecture notes on Langmuir probe diagnostics *Contrib. Plasma Phys.* **52** 295–308

Chung H-K, Song M-Y, Kwon J-W, Lee M-G, Park J, Bae N, Song J, Kim G-H, Ralchenko D and Ralchenko Y 2021

Population kinetics modeling of low-temperature argon plasma *Atoms* **9** 100
Deng Y, Han X, Rehman S-ur-R and Liu Y 2008 Modeling characteristics of nonequilibrium processes during breakdown of capacitive RF argon glow discharge *Phys. Plasmas* **15** 053507
Deutsch H, Becker K, Grum-Grzhimailo A N, Bartschat K, Summers H, Probst M, Matt-Leubner S and Märk T D 2004 Calculated cross sections for the electron-impact ionization of excited argon atoms using the DM formalism *Int. J. Mass Spectrom.* **233** 39–43
Donkó Z 2011 Particle simulation methods for studies of low-pressure plasma sources *Plasma Sources Sci. Technol.* **20** 024001
Donkó Z, Hartmann P, Korolov I, Schulenberg D, Rohr S, Rauf S and Schulze J 2023 Metastable argon atom kinetics in a low-pressure capacitively coupled radio frequency discharge *Plasma Sources Sci. Technol.* **32** 065002
Donkó Z, Tsankov T V, Hartmann P, Arellano F J T, Czarnetzki U and Hamaguchi S 2024 Self-consistent calculation of the optical emission spectrum of an argon capacitively coupled plasma based on the coupling of particle simulation with a collisional-radiative model *J. Appl. Phys.* **57** 375209
Drawin H W 1968 Zur formelmäßigen darstellung des ionisierungsquerschnitts für den atom-atomstoß und über die ionen-elektronen-rekombination im dichten neutralgas *Z. Phys. A* **211** 404–17
Drawin H W and Emard F 1973 Atom-atom excitation and ionization in shock waves of the noble gases *Phys. Lett.* A **43** 333–5
Druyvesteyn M J 1930 Der Niedervoltbogen *Z. Phys.* **64** 781–98
E Gogolides and H H Sawin 1992 Continuum modeling of radio-frequency glow discharges. I. theory and results for electropositive and electronegative gases *J. Appl. Phys.* **72** 3971–87
Economou D J 2017 Hybrid simulation of low temperature plasmas: a brief tutorial *Plasma Process. Polym.* **14** 1600152
Ellis H W, Pai R Y, McDaniel E W, Mason E A and Viehland L A 1976 Transport properties of gaseous ions over a wide energy range *At. Data Nucl. Data Tables* **17** 177–210
Engeln R, Klarenaar B and Guaitella O 2020 Foundations of optical diagnostics in low-temperature plasmas *Plasma Sources Sci. Technol.* **29** 063001
Fernando M, Almgren-Bell J, Oliver T, Moser R, Varghese P, Raja L and Biros G 2025 Boltzsim: a fast solver for the 1D-space electron Boltzmann equation with applications to radio-frequency glow discharge plasmas (arXiv:2502.16555)
Fernando M, Bochkov D, Almgren-Bell J, Oliver T, Moser R, Varghese P, Raja L and Biros G 2024 A fast solver for the spatially homogeneous electron Boltzmann equation (arXiv:2409.00207)
Ferrari R L 1965 Plasma diagnostic techniques. Edited by R. H. Huddlestone and S. L. Leonard. Academic Press, 1965, pp. 627, $19.50 *J. Plasma Phys.* **1** 156
Gangwar R K, Sharma L, Srivastava R and Stauffer A D 2012 Argon plasma modeling with detailed fine-structure cross sections *J. Appl. Phys.* **111** 053307
Gao N, Xi Y-B, Li J-J and Liu Y 2021 Fluid modeling on effects of discharge parameters on ionization in capacitive radio frequency argon discharges at low pressure *Vacuum* **192** 110466
Godyak V A 1990 Measuring EEDF in gas discharge plasmas
Godyak V A and Alexandrovich B M 2015 Comparative analyses of plasma probe diagnostics techniques *J. Appl. Phys.* **118** 233302
Godyak V A, Piejak R B and Alexandrovich B M 2002 Electron energy distribution function measurements and plasma parameters in inductively coupled argon plasma *Plasma Sources Sci. Technol.* **11** 525
Gogolides E and Sawin H H 1992 Continuum modeling of radio-frequency glow discharges. II. parametric studies and sensitivity analysis *J. Appl. Phys.* **72** 3988–4002
Gogolides E, Sawin H H and Brown R A 1992 Direct calculation of time-periodic states of continuum models of radio-frequency plasmas *Chem. Eng. Sci.* **47** 3839–55
Golubovskii Y, Gorchakov S and Uhrlandt D 2013 Transport mechanisms of metastable and resonance atoms in a gas discharge plasma *Plasma Sources Sci. Technol.* **22** 023001
Graves D B 1987 Fluid model simulations of a 13.56-MHz RF discharge: time and space dependence of rates of electron impact excitation *J. Appl. Phys.* **62** 88–94
Graves D B and Jensen K F 1986 A continuum model of DC and RF discharges *IEEE Trans. Plasma Sci.* **14** 78–91
Grigorian G M, Dyatko N A and Kochetov I V 2015 Experimental and theoretical study of the radial distribution of $Ar(^3P_0)$ metastable atoms in a DC glow discharge in argon *J. Phys. D: Appl. Phys.* **48** 445201
Gudmundsson J T, Krek J, Wen D-Q, Kawamura E and Lieberman M 2021 Surface effects in a capacitive argon discharge in the intermediate pressure regime *Plasma Sources Sci. Technol.* **30** 125011
Hagelaar G and Pitchford L C 2005 Solving the Boltzmann equation to obtain electron transport coefficients and rate coefficients for fluid models *Plasma Sources Sci. Technol.* **14** 722–33
Haugsjaa P O and Amme R C 1970 Ionization and metastable excitation in low-energy collisions of ground-state argon atoms *J. Chem. Phys.* **52** 4858–66
Hegerberg R, Elford M T and Skullerud H R 1982 The cross section for symmetric charge exchange of Ne+ in Ne and Ar^+ in Ar at low energies *J. Phys. B: At. Mol. Phys.* **15** 797–811
Helm H and Elford M T 1977 The mobility of Ar^+ ions in argon and the effect of spin-orbit coupling *J. Phys. B: At. Mol. Phys.* **10** 3849–51
Hernández-Ávila J, Basurto E and De Urquijo J 2004 Electron transport and ionization in CHF_3–Ar and CHF_3–N_2 gas mixtures *J. Phys. D: Appl. Phys.* **37** 3088–92
Kapper M G and Cambier J-L 2011 Ionizing shocks in argon. Part I: collisional-radiative model and steady-state structure *J. Appl. Phys.* **109** 113308
Katsonis K and Drawin H W 1980 Transition probabilities for argon (I) *J. Quant. Spectrosc. Radiat. Transfer* **23** 1–55
Kramida A, Ralchenko Y and Reader J (NIST ASD Team) 2023 *NIST Atomic Spectra Database (Version 5.11)* (National Institute of Standards and Technology) (https://doi.org/10.18434/T4W30F)
Kushner M J 2009 Hybrid modelling of low temperature plasmas for fundamental investigations and equipment design *J. Phys. D: Appl. Phys.* **42** 194013
Laguna A A, Esteves B, Raimbault J, Bourdon A and Chabert P 2023 Discussion on the transport processes in electrons with non-Maxwellian energy distribution function in partially-ionized plasmas *Plasma Phys. Control. Fusion* **65** 054002
Laguna A A, Hara K, Berger A, Bourdon A and Chabert P 2024 High-order moment closures for fluid models in weakly-ionized plasmas *Bull. Am. Phys. Soc.*
Lieberman M A and Lichtenberg A J 2005 *Principles of Plasma Discharges and Materials Processing* 2nd edn (Wiley)
Lin Y-h and Adomaitis R A 2001 Simulation and model reduction methods for an RF plasma glow discharge *J. Comput. Phys.* **171** 731–52
Lipka P, Mensah S, Gordon M and Bhat D 2007 Absolute argon excited-state population measurements from emission spectroscopy in an inverted cylindrical magnetron plasma *Surf. Coat. Technol.* **202** 910–4
Liu Q, Liu Y, Samir T and Ma Z 2014 Numerical study of effect of secondary electron emission on discharge characteristics in low

pressure capacitive RF argon discharge *Phys. Plasmas* **21** 083511
Liu R, Liu Y, Jia W and Zhou Y 2017 A comparative study on continuous and pulsed RF argon capacitive glow discharges at low pressure by fluid modeling *Phys. Plasmas* **24** 013517
Lymberopoulos D P and Economou D J 1993 Fluid simulations of glow discharges: Effect of metastable atoms in argon *J. Appl. Phys.* **73** 3668–79
Mahadevan S and Raja L L 2010 Simulations of direct-current air glow discharge at pressures 1 torr: Discharge model validation *J. Appl. Phys.* **107** 093304
McMillin B K and Zachariah M R 1995 Two-dimensional argon metastable density measurements in a radio frequency plasma reactor by planar laser-induced fluorescence imaging *J. Appl. Phys.* **77** 5538–44
Mitchner M and Kruger C H. 1973 *Partially Ionized Gases* (Wiley)
Mott-Smith H and Langmuir I 1926 Theory of collectors *Phys. Rev.* **28** 727–63
O'Connor R J, Fries D and Varghese P L 2025 Measurements of argon 4p state population densities in a capacitively coupled discharge *J. Appl. Phys.* **58** 285205
Ochkin V N 2009 *Spectroscopy of low Temperature Plasma* (Wiley)
Oxenius J 2012 *Kinetic Theory of Particles and Photons: Theoretical Foundations of non-LTE Plasma Spectroscopy* vol 20 (Springer)
Peshl J, McNeill R, Sukenik C I, Nikolić M, Popović S and Vušković L 2019 Argon metastable and resonant level densities in Ar and Ar/Cl_2 discharges used for the processing of bulk niobium *J. Appl. Phys.* **126** 103302
Phelps A V 1991 Cross sections and swarm coefficients for nitrogen ions and neutrals in N2 and argon ions and neutrals in Ar for energies from 0.1 eV to 10 keV *J. Phys. Chem. Ref. Data* **20** 557–73
Phelps A and Petrovic Z L 1999 Cold-cathode discharges and breakdown in argon: surface and gas phase production of secondary electrons *Plasma Sources Sci. Technol.* **8** R21
Raizer Y P, Shneider M N and Yatsenko N A 1995 *Radio-Frequency Capacitive Discharges* (CRC press)
Ralchenko Y 2016 *Modern Methods in Collisional-Radiative Modeling of Plasmas* (Springer)
Rossnagel S M, Cuomo J J and Westwood W D 1990 *Handbook of Plasma Processing Technology: Fundamentals, Etching, Deposition and Surface Interactions* (Noyes Publications)
Samir T, Liu Y and Zhao L 2018 Study on effect of neutral gas pressure on plasma characteristics in capacitive RF argon glow discharges at low pressure by fluid modeling *IEEE Trans. Plasma Sci.* **46** 1738–46
Tiwari P K, Kumar R, Halder K and Lee Y S 2023 Maxwell–Boltzmann and Druyvesteyn distribution functions expressing the particle velocity and the energy in sheath plasmas *J. Russ. Laser Res.* **44** 504–12
Van Sijde B D, Van der Mullen J and Schram D 1984 Collisional radiative models in plasmas *Beitr. Plasmaphys.* **24** 447–73
Verboncoeur J P 2005 Particle simulation of plasmas: review and advances *Plasma Phys. Control. Fusion* **47** A231
Viehland L A and Kirkpatrick C C 1995 Relating ion/neutral reaction rate coefficients and cross-sections by accessing a database for ion transport properties *Int. J. Mass Spectrom. Ion Process.* **149** 555–71
Vlček J 1989 A collisional-radiative model applicable to argon discharges over a wide range of conditions. I. formulation and basic data *J. Phys. D: Appl. Phys.* **22** 623–31
Vlček J and Pelikan V 1989 A collisional-radiative model applicable to argon discharges over a wide range of conditions. II. Application to low-pressure, hollow-cathode arc and low-pressure glow discharges *J. Phys. D: Appl. Phys.* **22** 632–43
Wen D-Q, Krek J, Gudmundsson J T, Kawamura E, Lieberman M A and Verboncoeur J P 2021 Benchmarked and upgraded particle-in-cell simulations of a capacitive argon discharge at intermediate pressure: The role of metastable atoms *Plasma Sources Sci. Technol.* **30** 105009
Wen D-Q, Krek J, Gudmundsson J T, Kawamura E, Lieberman M A, Zhang P and Verboncoeur J P 2023 On the importance of excited state species in low pressure capacitively coupled plasma argon discharges *Plasma Sources Sci. Technol.* **32** 064001
Wen Y-Y, Zhang Y-R, Jiang G, Song Y-H and Wang Y-N 2019 Secondary electron effect on sustaining capacitively coupled discharges: a hybrid modeling investigation of the ionization rate *AIP Adv.* **9** 055019
Zatsarinny O 2006 BSR: B-spline atomic R-matrix codes *Comput. Phys. Commun.* **174** 273–356
Zatsarinny O and Bartschat K 2006 B-spline calculations of oscillator strengths in neutral argon *J. Phys. B: At. Mol. Opt. Phys.* **39** 2145–58
Zhiglinsky A 1994 Handbook of constants of elementary processes with atoms, ions, electrons and photons *Saint Petersburg*
Zhu X-M and Pu Y-K 2010 A simple collisional–radiative model for low-temperature argon discharges with pressure ranging from 1 Pa to atmospheric pressure: kinetics of Paschen 1S and 2P levels *J. Phys. D: Appl. Phys.* **43** 015204
Zhu X-M, Tsankov T V, Luggenhölscher D and Czarnetzki U 2015 2D collisional-radiative model for non-uniform argon plasmas: with or without 'escape factor *J. Phys. D: Appl. Phys.* **48** 085201
Zhu X and Pu Y 2011 Determination of non-Maxwellian electron energy distributions in low-pressure plasmas by using the optical emission spectroscopy and a collisional-radiative model *Plasma Sci. Technol.* **13** 267–78